



# CO<sub>2</sub>QUEST Newsletter



Autumn 2014



## CO<sub>2</sub>QUEST

Impact of the Quality of CO<sub>2</sub> on Storage and Transport

### Introduction

Welcome to the second edition of the EU FP7-funded-project CO<sub>2</sub>QUEST newsletter, highlighting the most recent technical developments since the project's commencement in March 2013. The CO<sub>2</sub>QUEST consortium, led by Prof. Haroun Mahgerefteh at University College London (UCL, UK) comprises 9 other partners: Bundesanstalt für Geowissenschaften und Rohstoffe (BGR, Germany), Uppsala University (UU, Sweden), Dalian University of Technology (DUT, PR China), Environmental & Water Resources Engineering Ltd. (EWRE, Israel), Imperial College London (ICL, London), Institut National de l'Environnement Industriel et des Risques (INERIS, France), National Centre for Scientific Research 'Demokritos' (NCSR, Greece), Onderzoekscentrum voor Aanwending van Staal (OCAS, Belgium), and the University of Leeds (UoL, UK).

CO<sub>2</sub>QUEST addresses the fundamentally important issues regarding the impact of the typical impurities in the gas or dense-phase CO<sub>2</sub> stream captured from fossil fuel power plants on its safe and economic transportation and storage. The above involves the determination of the important CO<sub>2</sub> mixtures that have the most profound impact on the pipeline pressure drop, compressor power requirements, pipeline propensity to ductile and brittle fracture propagation, corrosion of the pipeline and wellbore materials, geochemical interactions within the wellbore and storage site, and the ensuing health and environmental hazards. Based upon a cost/benefit analysis and whole system approach, the results will in turn be used to provide recommendations for tolerance levels, mixing protocols and control measures for pipeline networks and storage infrastructure.

### Project Partners



University College London, UK



Bundesanstalt für Geowissenschaften und Rohstoffe, Germany



UPPSALA  
UNIVERSITET

Uppsala Universitet, Sweden



Dalian University of Technology,  
China



Environmental & Water Resources  
Engineering Ltd., Israel

Imperial College  
London

ICL, UK



Institut National de l'Environnement  
Industriel et des Risques, France



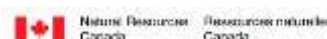
Demokritos, National Research  
Centre for Physical Sciences, Greece



Onderzoekscentrum voor  
Aanwending van Staal, Belgium



University of Leeds, UK



Canada

CanmetENERGY, Canada

# Pipeline Pressure Drop and Compressor Requirements

**S. Martynov, S. Brown, and H. Mahgerefteh**

*University College London, UK*

UCL is developing steady-state and transient-flow computational fluid dynamic (CFD) models for pipeline networks, to study the impact of impurities in the CO<sub>2</sub> stream on the flow behaviour during normal operation and pipeline failure. The latter involves coupling of the pipeline decompression code with a model representing running pipeline fracture, which is being developed by OCAS.

## Compressor Power Requirements

Minimising the pressure drop and avoiding two-phase flows within CO<sub>2</sub> pipeline networks are essential for reducing compressor power requirements. This is critically important given that the compression penalty for CO<sub>2</sub> capture from coal-fired power plants is estimated to be as high as 12% [1].

In order to evaluate the impact of CO<sub>2</sub> impurities on compressor power requirements, a thermodynamic analysis method is applied to CO<sub>2</sub> streams captured using oxy-fuel, pre-combustion and post-combustion capture technologies, the

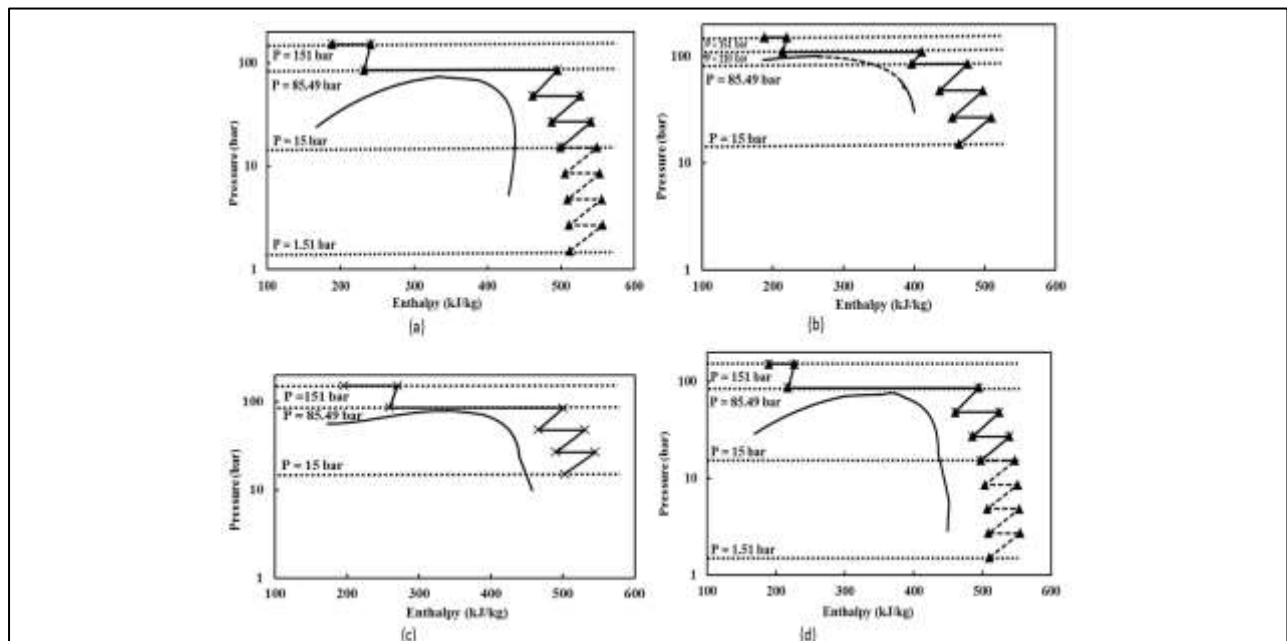
compositions of which are detailed in Table 1. The analysis is performed for several methods of compression previously recommended for pure CO<sub>2</sub>, including the following options [2]:

- **Option A:** Using the centrifugal integrally-gearred multistage compressors.
- **Option B:** Using supersonic axial compressors.
- **Option C:** Using compressors combined with liquefaction followed by pumping.

	Oxy-fuel	Pre-combustion	Post-combustion
<b>CO<sub>2</sub> (% v/v)</b>	<b>81.344</b>	<b>98.066</b>	<b>99.664</b>
O <sub>2</sub> (% v/v)	6.000	-	0.0035
N <sub>2</sub> (% v/v)	8.500	0.0200	0.2900
Ar (% v/v)	4.000	0.0180	0.0210
NO <sub>2</sub> (ppmv)	609.0	-	38.800
SO <sub>2</sub> (ppmv)	800.0	700.00	67.100
H <sub>2</sub> O (ppmv)	100.0	150.00	100.00
CO (ppmv)	50.00	1300.0	10.000
H <sub>2</sub> S (ppmv)	-	1700.0	-
H <sub>2</sub> (ppmv)	-	15000	-
CH <sub>4</sub> (ppmv)	-	110.00	-

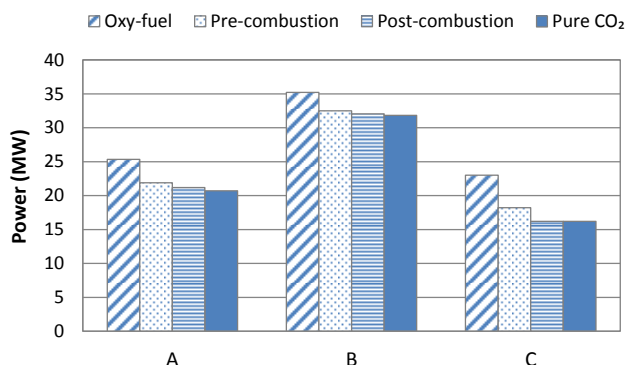
**Table 1.** Compositions of CO<sub>2</sub> mixtures captured from oxy-fuel, pre- and post-combustion technologies, adopted in the present study [3].

Fig. 1 shows an example of calculation of thermodynamic paths of multi-stage compression combined with intercooling relative to the phase envelopes for pure and impure CO<sub>2</sub> streams,



**Figure 1.** The thermodynamic paths for compression of pure CO<sub>2</sub> (a), and CO<sub>2</sub> mixtures from oxy-fuel (b), pre-combustion (c), and post-combustion (d) capture, using compression and pumping with supercritical liquefaction. Note that the compressor inlet pressure is 1.5 bar for pure CO<sub>2</sub> and post-combustion streams, and 15 bar for the pre-combustion and oxy-fuel streams.

whilst Fig. 2 shows the power consumption for each compression strategy (options A, B and C) for mixtures indicative of all capture technologies.



**Figure 2.** Power demand for multistage compression (options A, B and C) of pure CO<sub>2</sub>, oxy-fuel (raw/dehumidified), pre- and post-combustion streams (Table 1).

In particular, Fig. 2 shows that in agreement with the data published in the literature, the integration of the multi-stage compression with liquefaction and pumping (Option C) can greatly decrease the total power consumption (combining the power of compression and inter-cooling) when compared to conventional gas-phase compression (Option A). This option is particularly attractive for compression of almost pure CO<sub>2</sub>, when liquefaction can be achieved using utility streams at 20 °C for a post-combustion mixture of purity 99.6 vol %, and 8 °C for a pre-combustion mixture (CO<sub>2</sub> purity approximately 98 vol %). At the same time, the cryogenic temperatures needed for liquefaction of oxy-fuel CO<sub>2</sub> streams carrying 74-85 vol% of impurities, may require use of extra power for refrigeration. Clearly, such information forms the foundation for practical optimization of CO<sub>2</sub> compression, which should not be performed in conjunction with other processes involved in CCS chain, such as the CO<sub>2</sub> capture and transport.

### Non-isothermal Steady State Flow Modelling

To evaluate the impact of CO<sub>2</sub> impurities on pressure drop in pipelines, UCL is applying a previously developed computer model for the calculation of one-dimensional, transient, compressible, multiphase flows in pipes. This model accounts for both flow and phase-dependent viscous friction, and heat transfer between the transported fluid and the pipeline

environment [4, 5]. The model is being applied to study the impact of variation in concentration of CO<sub>2</sub> stream impurities at the inlets of a hypothetical pipeline network, upon the pressure and temperature profiles along the pipeline and the delivery composition for a given flow-rates and temperatures of the feed streams.

Fig. 3 shows an example of the considered realistic pipeline network, transporting CO<sub>2</sub> from Cottam and Drax power stations to the sequestration point at Morecambe South in the East Irish Sea.



**Figure 3.** UK CCS network, 2010-2020.

For a pipeline network configuration shown in Figure 3 the analysis of the steady-state pressure drop and temperature profiles has been performed for CO<sub>2</sub> mixtures carrying various impurities, including water, argon, nitrogen and oxygen, which are typically present in the oxy-fuel combustion CO<sub>2</sub> stream.

The model developed can be applied to perform sensitivity studies to identify impurities having the most adverse impact on the CO<sub>2</sub> pipeline transport.

# Predicting PVT CO<sub>2</sub>-brine Mixtures Behavior using ePC-SAFT with Application to CO<sub>2</sub> Geological Storage

G. Boulougouris, D.M. Tsangaris, and  
I. Economou

National Centre for Scientific Research  
Demokritos (NCSR), Greece

Accurate modelling of the storage of CO<sub>2</sub> injected into subsurface formations requires accurate and efficient fluid property models. Currently, NCSR is working on the development of an equation of state (EoS) based upon the Perturbed Chain-Statistical Associating Fluid Theory (PC-SAFT) that accounts explicitly for electrostatic (Coulombic) interactions that occur in CO<sub>2</sub>-brine (H<sub>2</sub>O-NaCl) mixtures.

Challenges arise in developing such a model due to the fact that electrostatic interactions are long-range intermolecular interactions that affect significantly the thermodynamic and transport properties, and the phase equilibria of the mixtures. Because of their long-range nature, special treatment is needed. Debye-Hückel theory, originally developed for close to infinite dilution electrolyte solutions, is incorporated in the PC-SAFT framework. The so-called electrolyte PC-SAFT (ePC-SAFT) is being developed and incorporated into the Physical Properties Library (PPL), the thermodynamic software package developed by NCSR during the CO2PipeHaz project (EC FP7 project number 241346).

The model developed in this work, is initially validated for the prediction of H<sub>2</sub>O-NaCl properties, namely density and phase equilibria, and is subsequently extended to the modelling of H<sub>2</sub>O-CO<sub>2</sub>-NaCl mixtures. Modelling results show that significant binary parameter adjustment is needed in order to obtain good agreement between literature experimental data and model correlations.

## Model description

PC-SAFT is a statistical mechanics based EoS rooted to perturbation theory, where the intermolecular potential is written as a sum of a reference (dominant) term and a perturbation term. Accordingly, the residual Helmholtz free energy,  $A^R$ , is written as a summation of contributions from different types of

intermolecular interactions, that include repulsive, dispersive and association (hydrogen bonding) interactions.

In the ePC-SAFT extension, explicit account of electrostatic interactions is included. As a result, ePC-SAFT is expressed as:

$$\frac{A^R}{RT} = \frac{A}{RT} - \frac{A^{ideal}}{RT} = \left( \frac{A^{hs}}{RT} + \frac{A^{chain}}{RT} + \frac{A^{disp}}{RT} + \frac{A^{assoc}}{RT} \right) + \frac{A^{ion}}{RT} \quad (1)$$

where  $T$  is the temperature,  $R$  is the gas constant and superscripts  $R$ ,  $hs$ ,  $disp$ ,  $chain$ ,  $assoc$  and  $ion$  indicate residual, hard sphere, dispersion, chain, association and ion-ion interactions. The individual terms are written in terms of temperature and density and can be found in recent publications from the NCSR group [6-8].

The ion-ion term is based on Debye-Hückel theory according to which:

$$\frac{A^{ion}}{RT} = -\frac{\kappa}{12\pi k_B T \epsilon} \sum_j x_j q_j^2 \chi_j \quad (2)$$

where  $x_j$  and  $q_j$  are the mole fraction and the charge of ion  $j$ , respectively, and  $k_B$  is the Boltzmann constant. The theory treats the solvent as a uniform dielectric continuum with dielectric constant ( $\epsilon$ ). Ions are spherical species that can approach each other to the distance  $a_j$  which is equivalent to the ion diameter  $\sigma_j$ . The quantity  $\chi_j$  in Eq. (2) is defined as:

$$\chi_j = \frac{3}{(\kappa a_j)^3} \left[ \frac{3}{2} + \ln(1 + \kappa a_j) - 2(1 + \kappa a_j) + \frac{1}{2}(1 + \kappa a_j)^2 \right] \quad (3)$$

and  $\kappa$  is the inverse Debye screening length given by:

$$\kappa = \sqrt{\frac{\rho_N e^2}{k_B T \epsilon} \sum_j z_j^2 x_j} \quad (4)$$

where  $\rho_N$  is the number density of the system and  $z_j$  is the charge number for ion  $j$ .

In PC-SAFT, pure non-associating fluids are characterized by three parameters that account



for the molecular size: 'm' which corresponds to the number of spherical segments per molecule; ' $\sigma$ ' which corresponds to the segment diameter; and the strength of intermolecular energy ( $\varepsilon/k_B$ ) that corresponds to the segmental potential energy parameter. For pure associating fluids (in this case H<sub>2</sub>O), two additional parameters are used for the associating energy per site ( $\varepsilon^{AB}/k_B$ ) and associating volume per site ( $\kappa^{AB}$ ). These parameters are typically fitted to experimental vapour pressure and liquid density data from low temperatures up to near the critical temperature. In addition, the number of associating sites per molecule varies from component to component.

Literature parameters were used in all calculations unless stated otherwise. For the case of water, two different models were tested:

- A 2-site model with parameters proposed in the original development of the PC-SAFT model for associating fluids [9]. This model will be referred to as H<sub>2</sub>O model 1.
- A 4-site model with parameters proposed by Diamantonis and Economou [10] that provided accurate correlation of H<sub>2</sub>O-CO<sub>2</sub> phase equilibria over a wide temperature range. This model is referred to as H<sub>2</sub>O model 2.

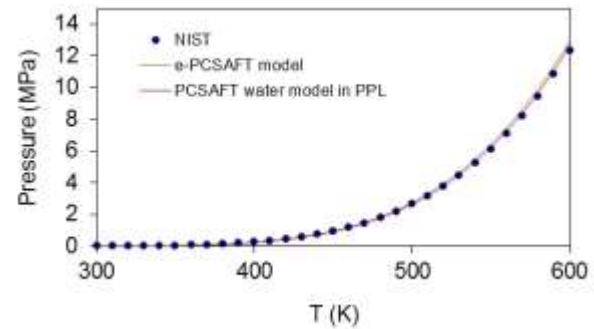
The parameters for all components examined are provided in Table 2.

### Model validation

#### Pure Component Property Predictions – The case of H<sub>2</sub>O

The newly implemented ePC-SAFT model was initially validated for pure H<sub>2</sub>O vapour pressure using experimental data [11]. In Figure 4, experimental data and predictions from the two sets of parameters of Table 2 are shown. The overall agreement of both of the models with experimental data is reasonable. The percent

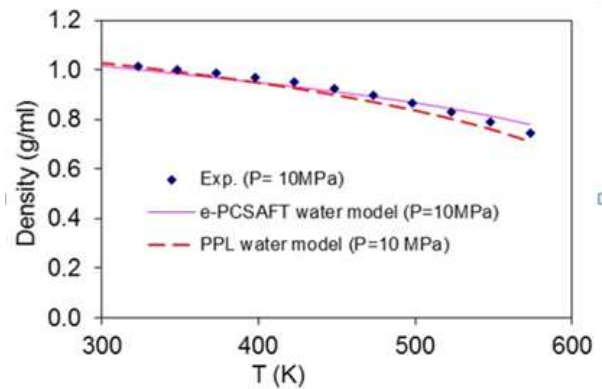
average absolute deviation (% AAD) is 1.91 % for the case of PC-SAFT and 2.84 % for the case of ePC-SAFT.



**Figure 4.** Vapour Pressure of H<sub>2</sub>O in the temperature

#### Binary Mixture Property Predictions – The case of H<sub>2</sub>O – NaCl

The ePC-SAFT model was tested for the prediction of density for H<sub>2</sub>O-NaCl mixtures at various temperatures and pressures. Experimental data and predictions from the two H<sub>2</sub>O models are shown in Figure 5 for pressure of 10 MPa at NaCl concentration of 0.5 M. In all cases, the agreement between experimental data and model predictions is very good. Similar results are obtained for pressure of 50 MPa.



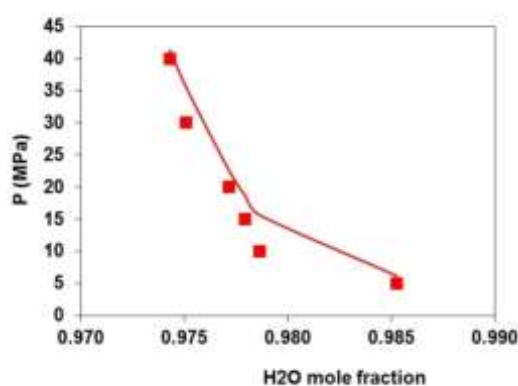
**Figure 5.** Density of 0.5 M NaCl aqueous solution at 10 MPa. Experimental data (points) [12], and ePC-SAFT predictions using Model 1 (solid line) Model 2 (dashed line).

Component	m	$\sigma$ (Å)	$\varepsilon/k_B$ (K)	$\varepsilon^{AB}/k_B$ (K)	$\kappa^{AB}$	$N_{\text{assoc}}$
H <sub>2</sub> O (1)	1.0656	3.001	366.512	2500.67	0.034868	2
H <sub>2</sub> O (2)	2.1945	2.229	141.66	1804.17	0.2039	4
CO <sub>2</sub>	2.6037	2.555	151.04	0	0	0
Na <sup>+</sup>	1	1.6262	119.806	0	0	0
Cl <sup>-</sup>	1	3.5991	359.66	0	0	0

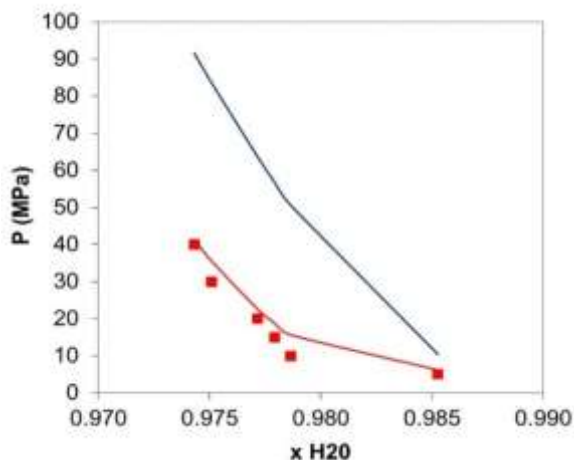
**Table 2.** PC-SAFT / ePC-SAFT pure component parameters for the components.

## Binary Mixture Property Predictions – The case of $H_2O$ - $CO_2$ .

The PC-SAFT accuracy to represent the  $H_2O$  –  $CO_2$  phase equilibria over a wide temperature and pressure range has been examined extensively by Diamantonis and Economou [10] who used different schemes to account for strong intermolecular interactions between  $H_2O$  and  $CO_2$  molecules. In Figure 6, experimental data and PC-SAFT predictions ( $k_{ij} = 0.0$ ) with model 2 for  $H_2O$  –  $CO_2$  VLE at 323.15 K are shown. The agreement between experiments and model is very good in all cases. Similarly, excellent agreement was obtained at 373.15 K and 413.15 K.



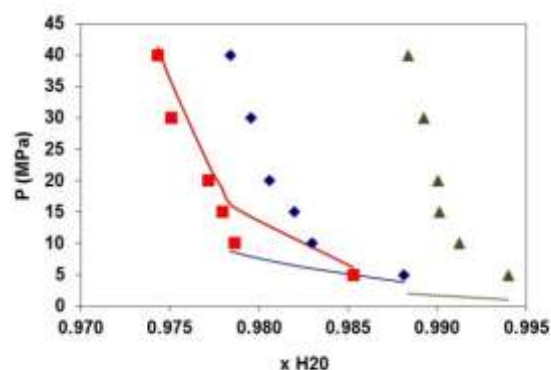
**Figure 6.**  $H_2O$ - $CO_2$  phase equilibria at 323.15 K. Experimental equilibrium pressure [13] (points) and PC-SAFT predictions (line) using model 2 for  $H_2O$ . On the other hand, Model 1 results show significant deviations from the experimental data (Figure 7) which raises questions about the accuracy of Model 1 when NaCl is added.



**Figure 7.**  $H_2O$ - $CO_2$  phase equilibria at 323.15 K. Experimental equilibrium pressure [13] (points), PC-SAFT predictions using model 2 for  $H_2O$  (red line) and PC-SAFT predictions using model 1 for  $H_2O$  (blue line).

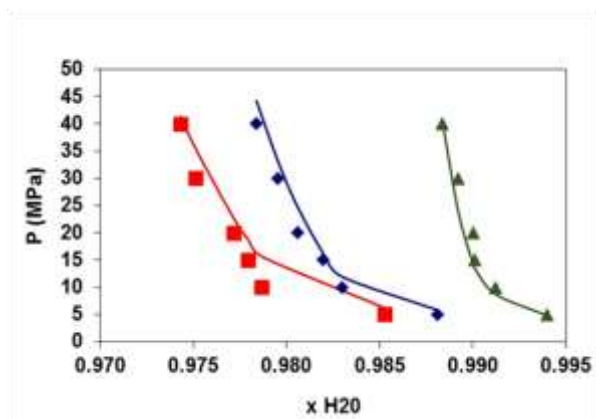
## Ternary Mixture Property Calculations: $H_2O$ - $CO_2$ -NaCl

The ultimate validation of the current development refers to the ternary  $H_2O$ - $CO_2$ -NaCl model. The starting point is the data shown in Figure 6 for the binary  $H_2O$ - $CO_2$  mixture. If one adds NaCl with increasing concentration, then the well known salting-out effect should be observed. Experimental data shown in Figure 8 for NaCl ( $M = 1$  and  $M = 5$ ) confirm this argument resulting in lower  $CO_2$  concentration at constant temperature and pressure. ePC-SAFT predictions with model 2 for  $H_2O$  (all three  $k_{ij} = 0.0$ ) result in the opposite effect. Similar results were obtained for the other two isotherms examined at 373.15 K and 413.15 K. We must mention here that Model 1 for  $H_2O$  results in similarly inaccurate predictions.

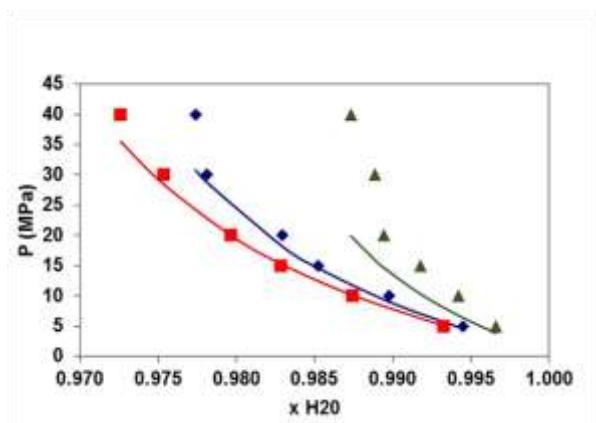


**Figure 8.**  $H_2O$ - $CO_2$ -NaCl phase equilibria at 323.15 K. Experimental data (points) [13] for NaCl = 0.0 M (red squares), 1.0 M (blue diamonds) and 5.0 M (green triangles) and ePC-SAFT predictions using model 2 for  $H_2O$  (lines).

In order to improve the model accuracy, a binary interaction parameter was added. Preliminary calculations reveal that a temperature dependent  $k_{ij}$  is needed for the  $CO_2$ - $Na^+$  and the  $CO_2$ - $Cl^-$  interactions. In Figures 9 and 10, experimental data and ePC-SAFT calculations at 323.15 K and 413.15 K, respectively, are shown for  $k_{CO_2-Na^+} = k_{CO_2-Cl^-} = 0.735$ . This  $k_{ij}$  value correlates well with the experimental data at 323.15 K but progressively becomes less accurate as temperature and NaCl concentration increase. At 413.15 K, a  $k_{ij}$  value of 0.95 is needed in order for ePC-SAFT calculations to agree with experiments. Clearly the model cannot capture the complex intermolecular interactions and additional work is needed.



**Figure 9.** H<sub>2</sub>O–CO<sub>2</sub>–NaCl phase equilibria at 323.15 K. Experimental data (points) [7] for NaCl = 0.0 M (red squares), 1.0 M (blue diamonds) and 5.0 M (green triangles) and ePC-SAFT correlations using model 2 for H<sub>2</sub>O and  $k_{\text{CO}_2\text{-Na}^+} = k_{\text{CO}_2\text{-Cl}^-} = 0.735$  (lines).



**Figure 10.** H<sub>2</sub>O–CO<sub>2</sub>–NaCl phase equilibria at 413.15 K. Experimental data (points) [7] for NaCl = 0.0 M (red squares), 1.0 M (blue diamonds) and 5.0 M (green triangles) and ePC-SAFT correlations using model 2 for H<sub>2</sub>O and  $k_{\text{CO}_2\text{-Na}^+} = k_{\text{CO}_2\text{-Cl}^-} = 0.735$  (lines).

### Conclusions and current work

An ePC-SAFT model has been developed and validated against experimental data and previous calculations from the NCSR group. *The work has revealed severe inaccuracies of ePC-SAFT model for the case of the ternary H<sub>2</sub>O–CO<sub>2</sub>–NaCl mixture.* A temperature-dependent binary interaction parameter is needed to match experimental data and model calculations. Thus, additional work is currently underway in order to improve modelling performance. Currently, the NCSR group evaluates the improved Debye-Hückel term proposed by Jiang and Adidharma [14] which appears promising for modelling salting out effects.

## Impact Profiles of Impurities

**R. Farret<sup>1</sup>, A. Ceroni<sup>1</sup>, Y. Flauw<sup>1</sup>, N. Shah<sup>2</sup> and P. Rivotti<sup>2</sup>**

<sup>1</sup> Institut National de l'Environnement Industriel et des Risques, France

<sup>2</sup> Imperial College London, UK

A number of FP7 projects have been initiated, concerned with the safety aspects along the CCS chain. The additional challenge in the CO<sub>2</sub>QUEST project is to identify and assess the incremental risk due to the presence of impurities in a CO<sub>2</sub> stream. A first step towards this objective is to undertake an impact-profile risk-analysis for each part of the CCS chain and each common impurity. This has been handled by partners at INERIS and ICL in the past few months.

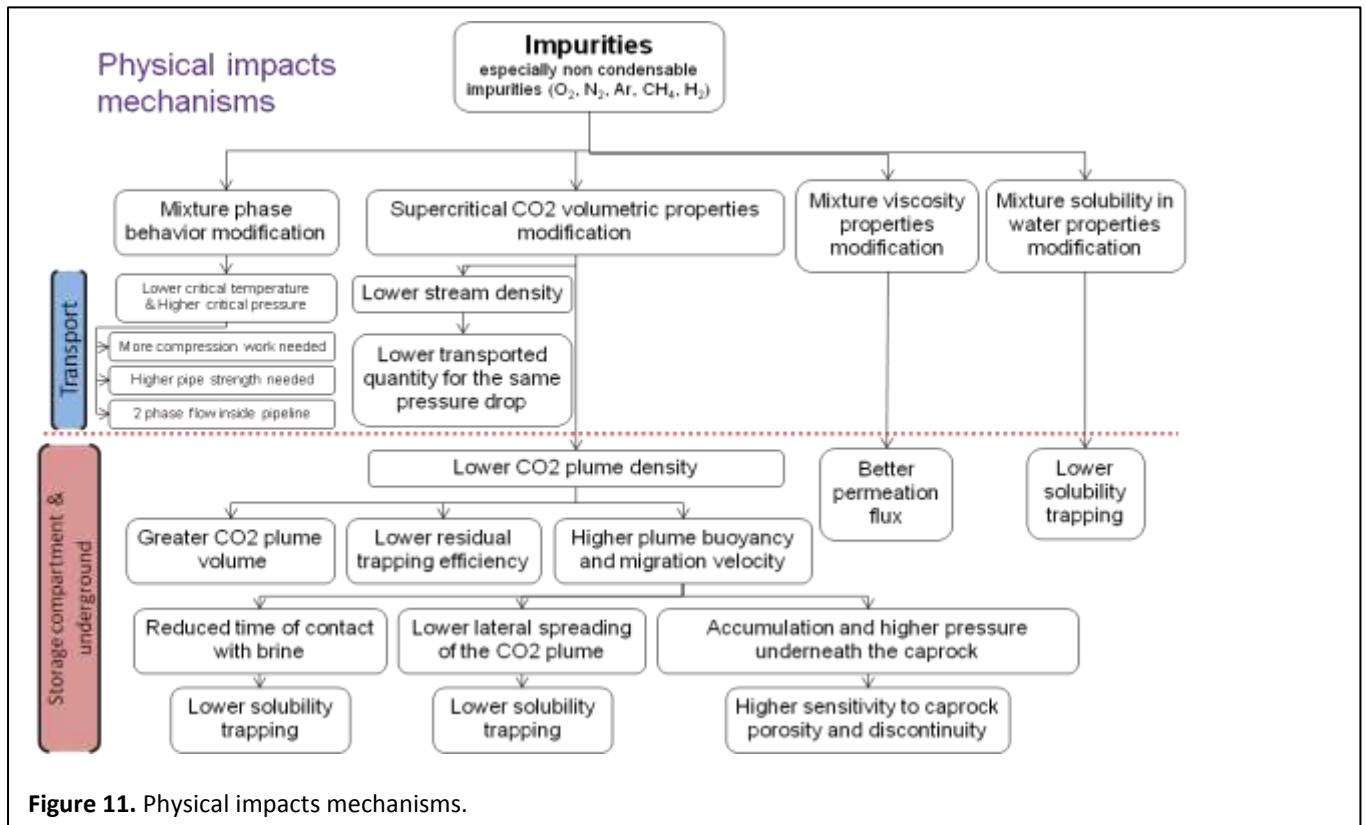
### Impacts mechanisms

To date, an overview of the current knowledge regarding the key effects of impurities along the CCS chain has been carried out. This also provides useful input to the design of a risk assessment and environmental analysis methodology, based upon the single and combined impurities effects. The work undertaken is based on a range of impurities identified by partners in another work package of the CO<sub>2</sub>QUEST project. For each impurity, its effects all along the CCS chain are identified via 3 categories of impacts:

- The physical impacts.
- The chemical impacts.
- The toxicological and ecotoxicological impacts.

### Physical impacts

Physical impacts of the impurities contained in captured CO<sub>2</sub> streams are a major concern for two main reasons. Firstly, the impurities responsible for these impacts are very common in the CO<sub>2</sub> streams produced from the main capture technologies (pre-combustion, post-combustion, and oxyfuel combustion). Secondly, the physical behaviour of the CO<sub>2</sub> stream has macroscopic impacts all along the CCS chain. In fact, by reducing the overall efficiency of the CCS application or by improving its global cost, physical effects of impurities could have major consequences, which have to be assessed and forecast. Figure 11 depicts example impact mechanisms.



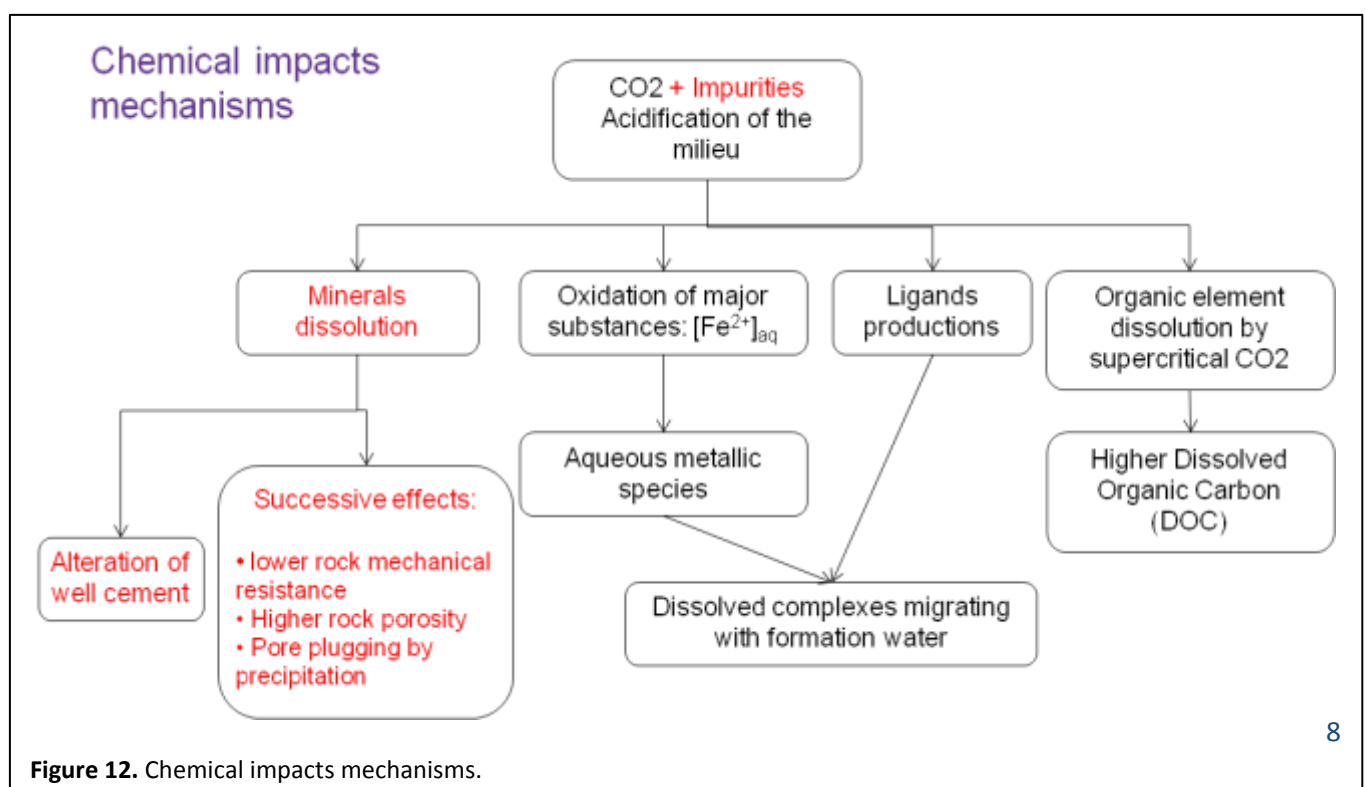
### Chemical impacts

During transport and storage, a  $CO_2$  stream experiences a number of different steps and physical conditions that can lead to significant chemical alterations. This alteration of  $CO_2$  properties on a chemical level can instigate unwanted subsequent reactions. Figure 12 highlights some of these possibilities.

### Toxical and ecotoxical impacts

Once injected into the storage environment,

potential impacts of the  $CO_2$  need to be considered on a long-term scale. Indeed, environmental impacts may still occur in the case of loss of containment. Such a loss can be a result of either an integrity default of the storage (fault through the caprock, existing or well) or too high caprock porosity. Concerning toxicity and environmental sensitivity, even low concentration of impurities may have significant impacts. Figure 13 graphically depicts some of the toxicity mechanisms.





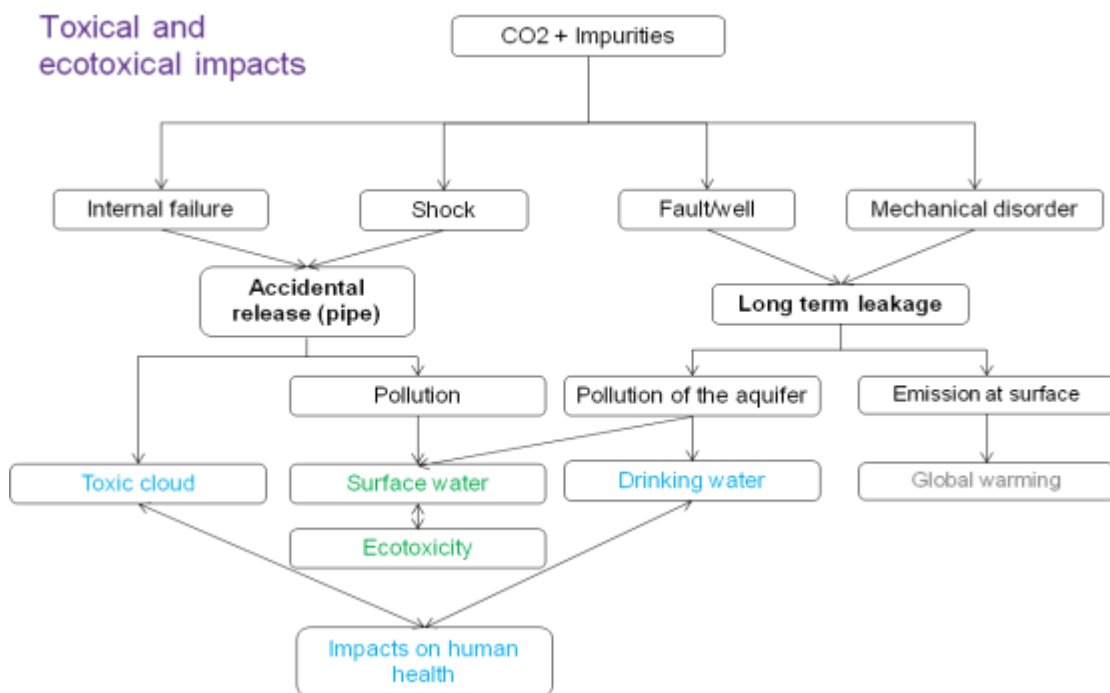


Figure 13. Toxic and ecotoxic mechanisms.

### Matrix tool

For each impurity identified by other partners as a common impurity, all the potential impacts described above are investigated and displayed in a matrix tool, with the concentration thresholds when relevant. An extract of this matrix tool is presented as Figure 14.

C39													
	A	B	C	D	E	F	G	H	I	J	K	L	M
	Impurity	Category of impact	Other relevant substances having the effect	Acid	Alkaline	Redox	Heavy metals	Organic compounds	Trace elements	CO2	Hydrocarbons	Other	Mechanism
Physical impacts	Physical impacts												
	1	Increased acid reactivity											Increases the CO2 reactivity towards the soil
	2	Increased acid reactivity											Increases the CO2 reactivity towards the soil
	3	Increased acid reactivity											Increases the CO2 reactivity towards the soil
	4	Increased acid reactivity											Increases the CO2 reactivity towards the soil
	5	Increased acid reactivity											Increases the CO2 reactivity towards the soil
	6	Increased acid reactivity											Increases the CO2 reactivity towards the soil
	7	Increased acid reactivity											Increases the CO2 reactivity towards the soil
	8	Increased acid reactivity											Increases the CO2 reactivity towards the soil
	9	Increased acid reactivity											Increases the CO2 reactivity towards the soil
	10	Increased acid reactivity											Increases the CO2 reactivity towards the soil
Chemical impacts	Chemical impacts												
	11	Hydrogen formation											Hydrogen formation
	12	Hydrogen formation											Hydrogen formation
	13	Hydrogen formation											Hydrogen formation
	14	Hydrogen formation											Hydrogen formation
	15	Hydrogen formation											Hydrogen formation
	16	Hydrogen formation											Hydrogen formation
	17	Hydrogen formation											Hydrogen formation
	18	Hydrogen formation											Hydrogen formation
	19	Hydrogen formation											Hydrogen formation
	20	Hydrogen formation											Hydrogen formation
Ecological impacts	Ecological impacts												
	21	Ecological impacts											
	22	Ecological impacts											
	23	Ecological impacts											
	24	Ecological impacts											
	25	Ecological impacts											
	26	Ecological impacts											
	27	Ecological impacts											
	28	Ecological impacts											
	29	Ecological impacts											
	30	Ecological impacts											

Figure 14. Matrix tool.

## Geochemical Impact on Impure CO<sub>2</sub> Storage Reservoir Integrity

**Jan Lennard Wolf and Dorothee Rebscher**

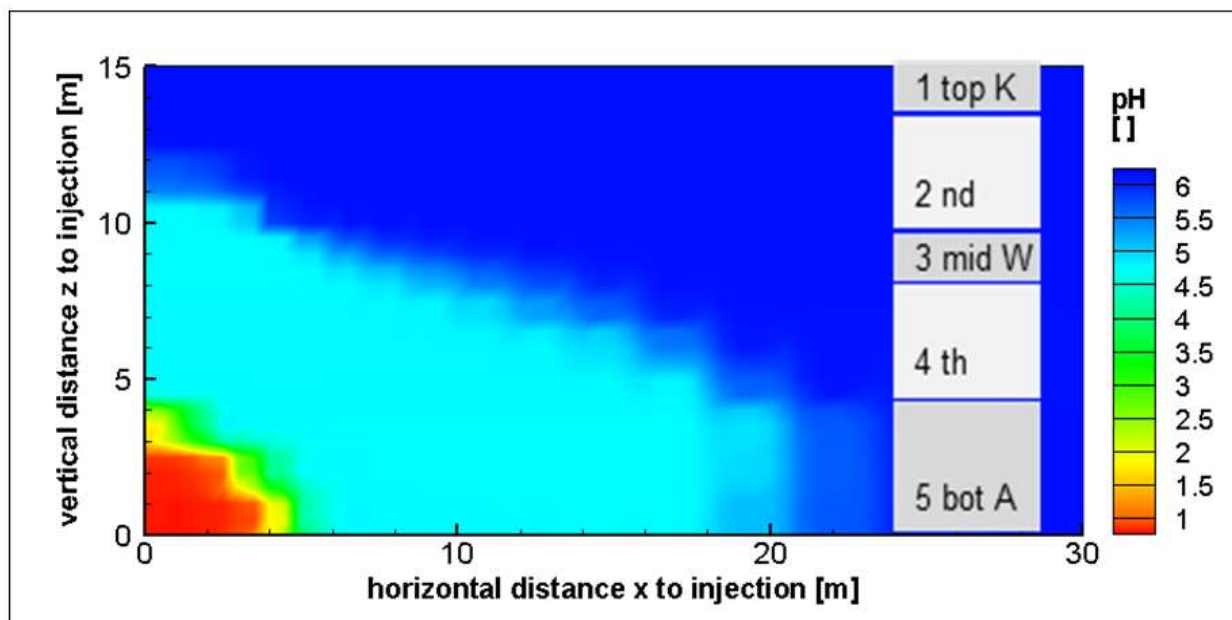
*Federal Institute for Geosciences and Natural Resources (BGR), Department of Subsurface Use, Geological CO<sub>2</sub> Storage, Hannover, Germany*

Workpackage 3 within the CO<sub>2</sub>QUEST project investigates the effects of impurities on the performance of geological storage of carbon dioxide. Here, push-pull injection tests conducted at the Heletz test site in Israel represent a prominent part. The study comprises design, implementation, and modelling. The objective is to enhance the understanding of changes in the characteristics of the reservoir during CO<sub>2</sub> injection in the presence of impurities. Physical or chemical reservoir properties can be influenced by nitrogen or sulfur dioxide, respectively. In this context, BGR focuses on the critical geochemical impacts of impure CO<sub>2</sub> on the deep saline aquifer.

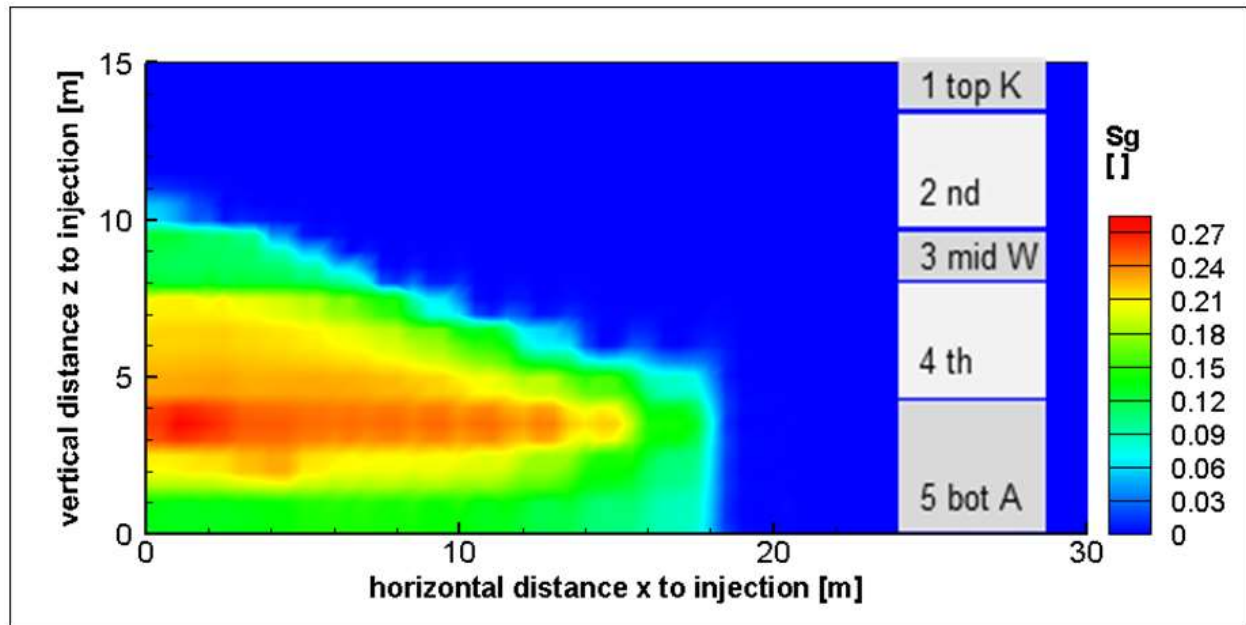
In close consultation with our partners at the University of Uppsala and Environmental and Water Resources Engineering, Haifa, a set of input parameters were agreed upon, backed by

data from Heletz field experiments, laboratory work, in addition to literature data. Based on this data set, a simple radially 2D model was constructed. The layers of interest in the Heletz saline aquifer comprise three sandstone layers and two adjacent shale layers, represented in the model by 15 × 50 cells. The numerical simulator TOUGHREACT with its module ECO2N is applied to simulate the relevant reactive transport processes, focussing on the chemical impacts of the impurity compound SO<sub>2</sub> on the brine-rock system in the target sandstone. During the first part of the simulation, CO<sub>2</sub> is injected at a rate of 0.28 kg/s, injected with 2 mol H<sub>2</sub>O dissolved SO<sub>2</sub> as impurity, and 0.0054 kg/s NaCl in order to fit the requirements of the simulator and maintain the saline environment. The injection phase covering a time span of 100 hours, is followed by a subsequent relaxation phase of 144 h.

As a first result, it can be verified that the areas of chemical impact of CO<sub>2</sub> and SO<sub>2</sub> are separated. The effect of SO<sub>2</sub> is characterised through the formation of sulphuric acid leading to a region of very low pH value in the vicinity of the injection well with a radial extent of approximately 5 m, as shown in Figure 15. The low pH value subsequently evokes a high reactivity of the minerals and intense release of metal ions as



**Figure 15.** In the radially 2D model, changes in pH value at the end of the relaxation phase show very low pH values close to the injection point after an injection phase with subsequent relaxation phase covering a time span of about 10 days and a coinjection of about 100 t CO<sub>2</sub> and 3 t SO<sub>2</sub>. In the vertical plane, changes in pH value reach the border between the highest shale layer 2 and the middle sand layer W at distances of approximately 10 m. The region defined by the multicoloured areas portrays the part of the storage formation affected by the push-pull test. The so far unaffected domain remains in the dark bluish background colour. Note that only the vicinity of the injection site is shown, as the whole lateral extent of the model covers 1000 m. In the vertical the highest pH values are found in the lowest sandstone layer 5, featuring a height of 4.



**Figure 16.** Spatial distribution of gas saturation  $S_g$  in the 2D model. After an injection phase with subsequent relaxation phase, the radial extent stretches to almost 20 m. In the vertical, the plume is constrained by the shale layer 2 at a vertical distance of about 10 m. The highest saturation is situated at the first contrast in permeability, directly below the border between sand layer A and shale layer 4 at 4.8 m.

mineral constituents. The influence of  $\text{CO}_2$  can be seen by the wider lateral extent of the gas saturation of the plume, with a spreading of almost 20 m, as in Figure 16. The physical impact due to injection, i.e. the pressure dissipation, is almost 10 times larger, amounting to approximately 200 m in its horizontal distance to the injection cell.

## Material Properties for Carbon Steel Pipeline Materials for CO<sub>2</sub> Transport

**D. Van Hoecke and S. Cooreman**

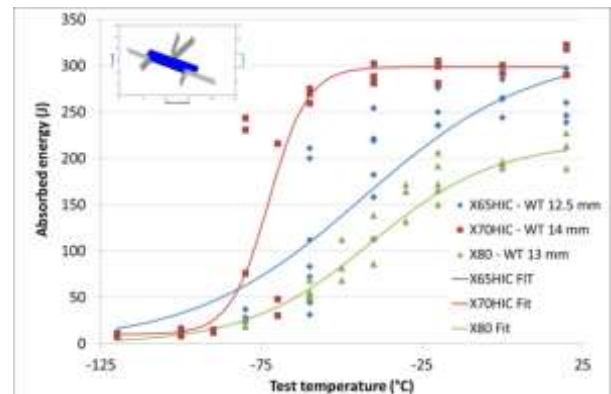
*Onderzoekscentrum voor Aanwending van Staal,  
OCAS N.V., Belgium*

As discussed in the previous newsletter, three different material grades are being characterised in the CO<sub>2</sub>QUEST project, namely X65, X70, and X80. The first two grades are already used in existing CO<sub>2</sub> pipelines, whilst the third grade (X80) is not yet in service. Investigating this material may provide some insights on its usability for CO<sub>2</sub> pipelines. Important aspects for material selection are:

- The response to impurities such as H<sub>2</sub>S which may cause sulfide stress cracking.
- Corrosion behaviour: The CO<sub>2</sub> stream is likely to contain impurities affecting the corrosion of pipelines and thus pipeline integrity. Samples of the selected steel grades have been prepared and are being exposed in a lab simulator of another project partner, to a CO<sub>2</sub> gas stream containing typical impurities to investigate the corrosion behaviour experimentally.
- Low temperature behaviour: A leak in a buried CO<sub>2</sub> pipeline can lead to substantial cooling of the surrounding soil lowering the pipe temperature.

To narrow down the material choice and select the most suitable for more detailed investigations, Charpy and Battelle drop weight tear tests were conducted on the three steel grades. The Charpy test results are given in Figure 17 which shows that the X70HIC material had the highest Charpy toughness, and if one takes into account the higher thickness of the test X70 material, it has a similar behaviour in Battelle testing. Since it is also relatively resistant to (accidental) H<sub>2</sub>S exposure, the X70HIC was selected for this project as the preferred choice

for more in-depth characterization and validation tests.



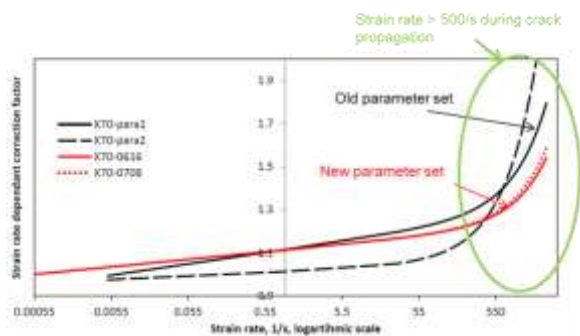
**Figure 17.** Transition curves for the three materials using Charpy samples.

The actual behaviour of the steel during a CO<sub>2</sub> pipeline failure is not likely to be predictable solely by Charpy and Battelle tests since it also depends on the gas decompression behaviour leading to specific fracture conditions for the material (i.e. temperature, stress concentrations, high deformation speeds, etc.). To tackle this in a universal approach, activities have concentrated upon:

- A numerical strategy to couple the hybrid ductile-brittle damage model used by OCAS to the CFD model of UCL describing the gas decompression.
- Improvement of the brittle fracture criterion.
- Fine tuning of the parameters of the damage model for the operating conditions typical for CO<sub>2</sub> pipeline failures.

The damage model was not optimally calibrated for high deformation speeds. Therefore, so-called Hopkinson bar experiments were carried out to quantify the material response at strain rates above 500 /s which can be observed during crack propagation. Figure 18 compares the fine tune correction function (red solid line) to the old correction function (black solid line).





**Figure 18.** Strain rate dependency in fracture model before and after new Hopkinson bar data.

As next steps the brittle fracture criterion will be implemented in the Abaqus damage model. The coupling of this model with the CFD model will be tested and optimised if necessary. Next to this the material and damage model predictions will be validated using medium scale crack propagation experiments and small and medium scale CO<sub>2</sub> release experiments by other partners on components containing an artificial defect.

## Medium Scale Experimental Investigation

**J. Hébrard, D. Jamois and C. Proust**

*Institut National de l'Environnement Industriel et des Risques, France*

INERIS is conducting controlled medium-scale experiments involving high pressure releases of CO<sub>2</sub> containing a range of impurities. The experimental rig and techniques developed during the CO<sub>2</sub>PipeHaz project [15, 16] have been re-used in order to establish a better understanding of the influence of the presence of impurities on both the flow inside the pipe and on the external dispersion. Measurements in the near-field and in the pipeline outflow will allow the further development of databases and will be used for the validation of mathematical models.

The rig and equipment developed in the CO<sub>2</sub>PipeHaz project is shown in Figure 19 (Left). This includes a 40 m long, 50 mm internal diameter pipeline, with pressure and temperature transducers placed along the tube at intervals of 10 meters. The near-field is also instrumented with pressure transducers and thermocouples. Equipment has also been especially developed to be adaptable to the study of the 'flash zone' and is shown in Figure 19 (Right).

A transparent section is also installed in the centre of the pipe, and the inside flow is



**Figure 19.** Left: View of the pipe resting on the weighing masts (blue); Right: near field equipment.

visualised during the release with a high speed camera. The pipe is filled via a pump, and the transparent section also permits a check upon the level of liquid CO<sub>2</sub> in the pipe.

A particular focus is made upon the mass flow-rate measurement. To this end, electronic measuring equipment records data at six weighing points. A weighing mast is visible in Figure 19 (Left). Two tests have been run with 100% of CO<sub>2</sub> liquid. The experimental conditions are presented on the next table:

Test n°		1	2
Pressure	[Bar]	55	65
Ambient temperature	[°C]	18	25
Orifice diameter	[mm]	6	12

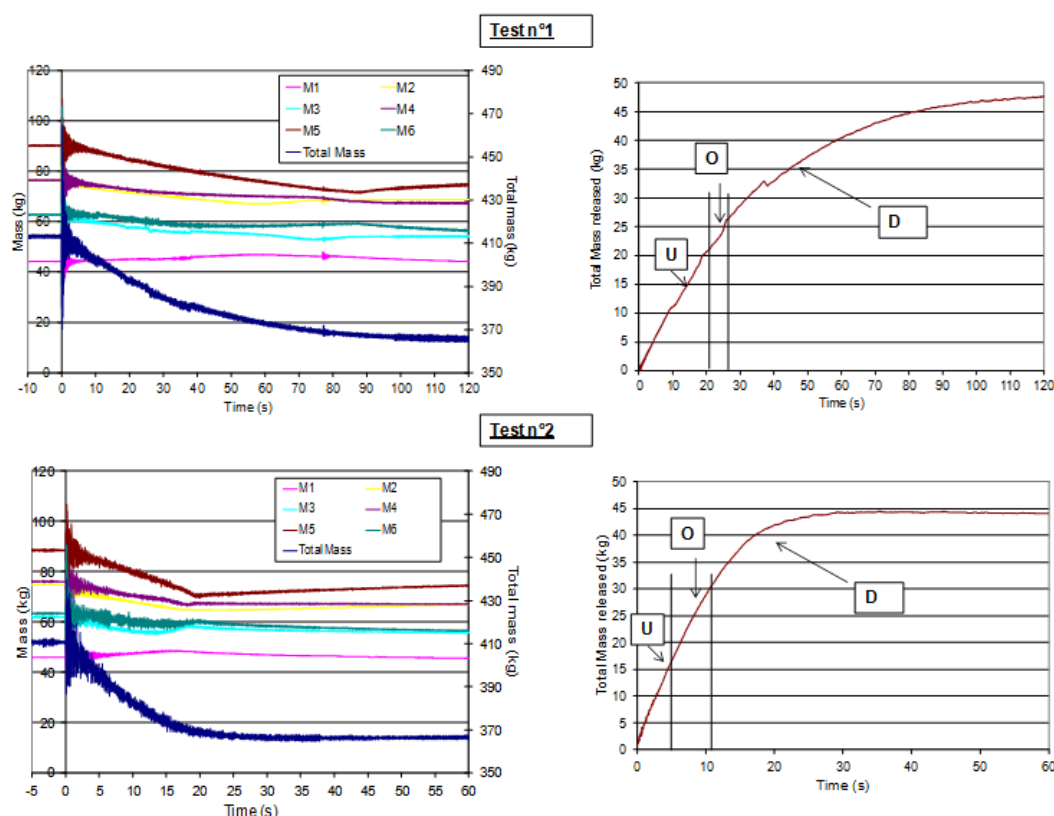
**Table 3.** Experimental conditions.

The evolution of the mass versus time, at each measurement point, is presented in Figure 20 for the two tests. Before the release, the total measured mass is not uniform over all measuring points, and ranges from 45 kg to 90 kg. These disparities can be explained by the presence of different equipment on the pipe (measurement, filling, mixing, transparent section).

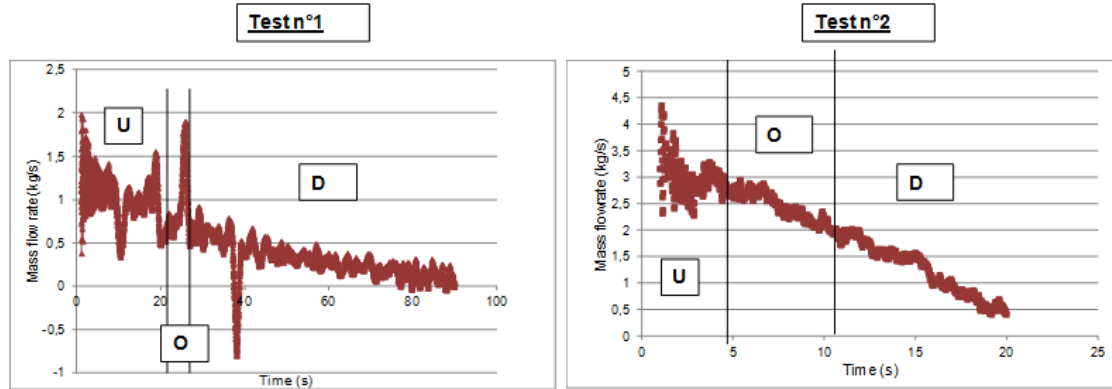
Figure 20 also presents the evolution of the mass released versus the time. The first period (a few hundred milliseconds after the start of the release) corresponds to the short time during which the fluid inside the pipe is nucleating but appears homogenous. The next period (21 s for test 1 and 5 s for test 2) corresponds to the period where a defined two-phase mixture is present in the pipe and the level of liquid is above the orifice (point U in Figure 20). Subsequently, the level of liquid reaches the orifice (O). After 26 s for test 1 and 11 s for test 2, the level of liquid is below the orifice (D). The two-phase flow ends after less than 2 minutes for test 1 and approximately 25 s for test 2 when the fluid becomes vapour.

The mass flow-rate measurement is crucial to the validation of the models [17], and its evolution is calculated by a temporal derivation of the mass released and is presented in Figure 21 for the two-phase flow. The different phases of the releases are identified on the figure depending upon the liquid level in the pipe.

Another issue for modellers is the assumption of adiabaticity. INERIS has added heat-flux meters to the skin of the pipe in order to measure the heat exchanges between it and the surroundings. An example of the evolution of the heat fluxes are presented for test 2 in Figure 22.



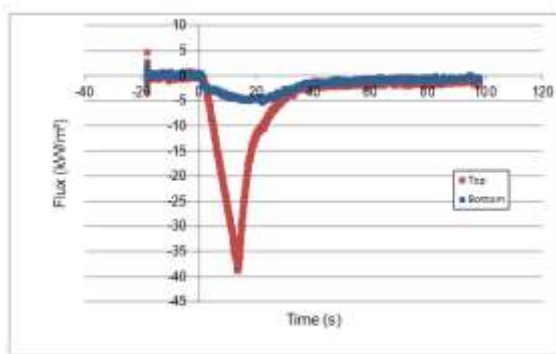
**Figure 20.** Evolution of total mass, and mass released, versus time.



**Figure 21.** Mass flowrate.

The blue line corresponds to the probe placed on the top of the pipe (gas), and the second probe is located on the bottom (red) corresponding to the liquid.

In addition, insulation has been added to the pipe in order to facilitate the interpretation of the experimental results and assist modellers.



**Figure 22.** Heat fluxes measured on the top and on the bottom of the pipe.

## Techno-economic Assessment

**N. Mac Dowell, N. Shah**

*Imperial College London, UK*

### Whole-systems modelling

Partners at Imperial College London are applying a multi-scale modelling approach to the analysis of a CO<sub>2</sub> capture and transport system. Focus is upon the development of a series of scale-specific models which interact across a range of length and time scales. This approach is particularly relevant to the CO<sub>2</sub>QUEST project as the hour-to-hour behaviour of the CO<sub>2</sub> sources within a given decarbonised bubble will dictate the flow-rate and composition of the CO<sub>2</sub> in the transport network. This modelling approach is illustrated in Figure 23 below.

As our energy system evolves, incorporating ever greater quantities of intermittent renewable energy, so too will the roles of the various generators which contribute to this system. This is illustrated in Figure 24. As can be seen, as we move from the 2030s to the 2050s and beyond, the role of CCS plants within the energy system significantly changes, and the ability to operate in a flexible, load-following manner becomes more valued.

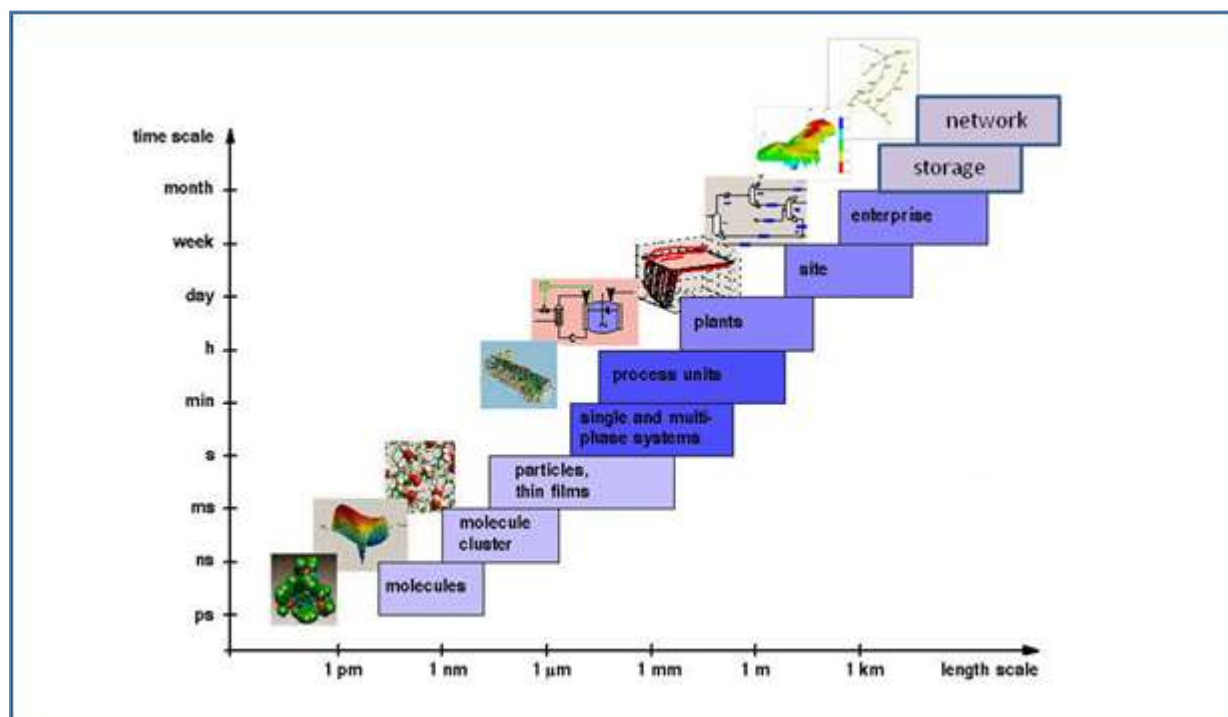
In our recent work , we have applied the theory

of Grossmann and Sargent [18] to dynamic, non-equilibrium models of a decarbonized power plant [19-26] and evaluate three distinct options for flexible operation:

1. Solvent storage – a portion of solvent is stored during periods of peak electricity demand and regenerated during off-peak periods
2. Exhaust gas venting – a portion of the exhaust gas is vented during periods of peak electricity demand
3. Time-varying solvent regeneration – CO<sub>2</sub> is allowed to accumulate in the working solvent during periods of peak electricity demand and the solvent is more thoroughly regenerated during off-peak periods

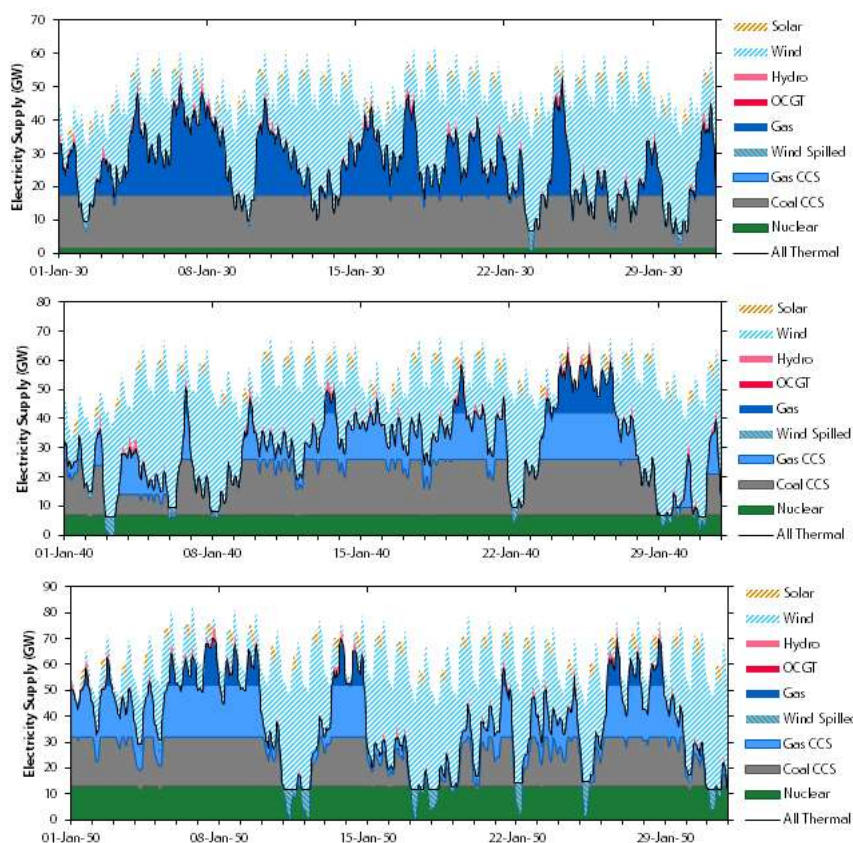
In all cases, we use a load-following power plant with post-combustion CO<sub>2</sub> capture as a reference case. We evaluate each option for flexible operation based upon the integrated degree of capture (IDoC) and cumulative profit realized by the power plant over the course of the simulation. Our economic considerations are based on both fuel (coal and gas) prices and a cost of CO<sub>2</sub> emission based on the carbon price floor proposed by the UK's Department of Energy and Climate Change . The time period we are considering is the early 2030s.

In this section, we present the results of our optimization problem. For all scenarios, the



**Figure 23.** Illustration of multi-scale modelling concept.





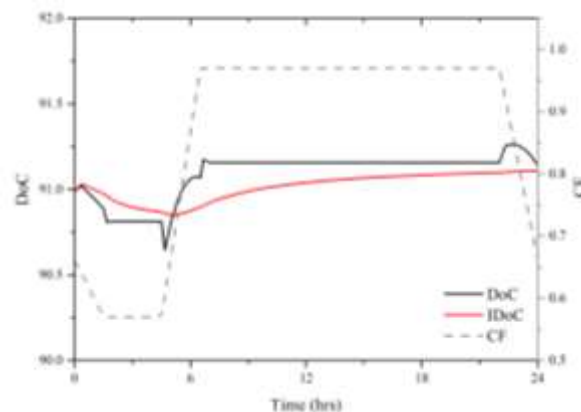
**Figure 24.** Evolution of operating patterns of the UK power generation system from 2030 to 2050 – output from MESMERISE project using the ETRC model.

optimization problem solved was the maximization of profit subject to the end point constraint of the IDoC being greater than or equal to 90 %.

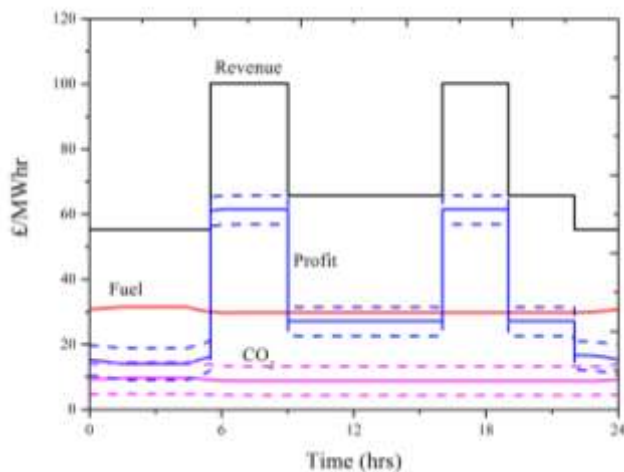
### Load-following

This was our benchmark scenario. Here, the capture plant was designed and the operating parameters specified via a steady state optimization as described in our previous paper [27]. We evaluated the effect of a multi-period dynamic optimization had on the end design of the plant. However, as the duration of the period for which the power plant is operating at full load is long relative to the period for which the power plant is operating at part load, the multi-period design was essentially identical to the steady state design, and the solution period of the steady state design problem was an order of magnitude faster than that of the multi-period problem. Thus, in this case, all operating parameters in the CO<sub>2</sub> capture plant, i.e., the L/G ratio, lean loading,  $\phi_{lean}$ , solvent inlet temperature,  $T_{In}^{Solv}$  etc., were held constant throughout the simulation.

It can be observed from Figure 25 that, as the capacity factor of the power plant changes, so too does the instantaneous degree of capture (DoC), albeit by a very small amount. This is associated with the changing gas and liquid flowrates in the absorption column leading to a variation in the effective surface area in the packed section. This implies that if the duration or frequency of periods of dynamic operation are long or great relative to the duration or frequency of periods of steady state operation, the IDoC could be reduced as a result.



**Figure 25.** Degree of CO<sub>2</sub> capture varying with power plant capacity factor (CF).

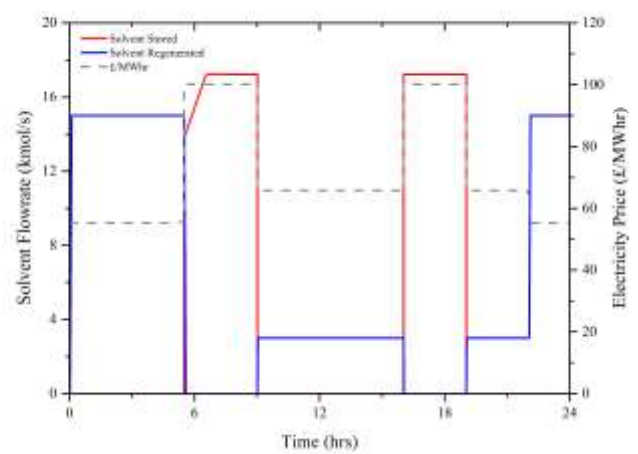


**Figure 26.** An analysis of the various financial streams associated with the generation of low carbon electricity in the case of conventional load following.

Illustrated in Figure 26, we provide an evaluation of the various financial streams associated with the power plant. It can be observed that the fuel cost per MWh is slightly increased during periods of operation at a low load factor in comparison with periods of operation at a high load factor. This is commensurate with the decreased efficiency of the power plant under this mode of operation. The cost associated with CO<sub>2</sub> emission is similarly elevated during this period, commensurate with the slightly reduced DoC as illustrated in Figure 31. Finally, as the plant is operating at an essentially constant degree of capture of approximately 90 %, it can be observed that the CO<sub>2</sub> price exerts an important influence on the profitability of the plant.

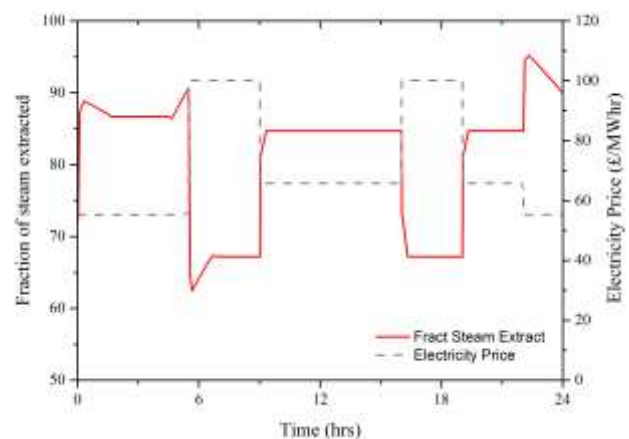
### Solvent storage

In this scenario, in order to decouple the operation of the power and capture plants, we consider the option of storing a fraction of the rich solvent during periods of peak electricity prices and subsequent regeneration of the solvent during periods of off-peak electricity prices. Here, the extra parameter to be determined is the quantity of solvent stored or regenerated in each time period. Therefore, this is a multi-period, piece-wise linear, dynamic optimisation problem. As can be observed, when electricity prices are lowest, the flow-rate of solvent to regeneration is greatest. Similarly, during periods of peak electricity price, rich solvent is directed to storage, bypassing the regeneration process



**Figure 27.** An analysis of the solvent storage and regeneration is presented here.

The advantage of the solvent storage strategy is that it reduces the quantity of steam required for solvent regeneration during key periods of peak electricity demand, as illustrated in Figure 28.

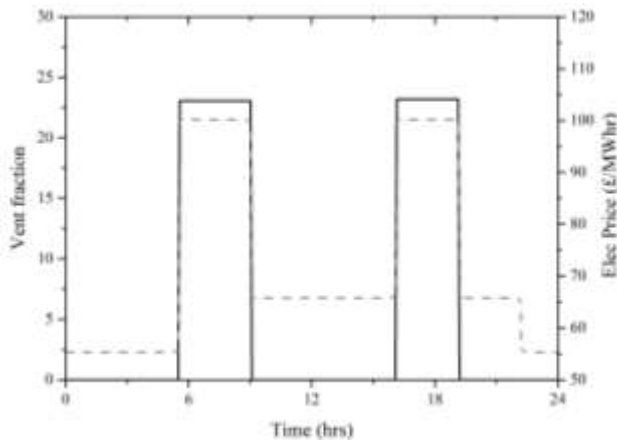


**Figure 28.** Steam requirement for solvent regeneration under the solvent storage option.

However, the availability of steam is a major constraint on the amount of solvent which can be stored during periods of peak electricity demand. It was a constraint in this problem that whatever solvent was stored during periods of peak electricity prices had to be regenerated during off-peak periods. This meant that it was only possible to store approximately 15 % of the total solvent flow. This corresponds to a cumulative volume of stored solvent of approximately 11,750 m<sup>3</sup> of solvent over both periods.

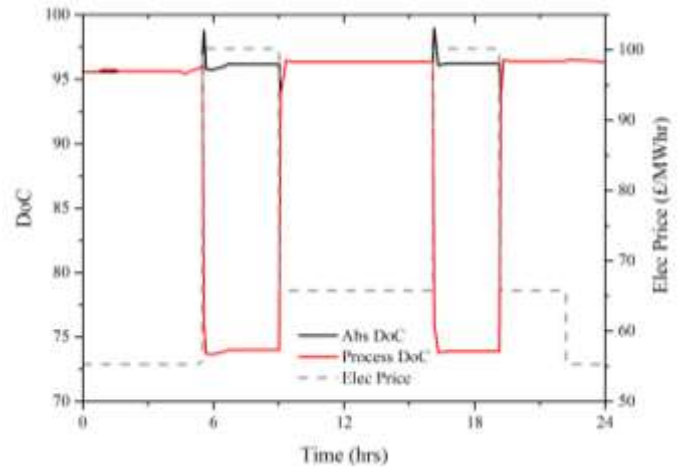
### Exhaust gas venting

In this scenario, the power plant ramps up and down, but in order to decouple the operation of the power and capture plants, we consider the option of venting a fraction of the exhaust gas during periods of peak electricity prices. Here, the extra parameter to be determined is the quantity of exhaust gas to be vented in each time period. Therefore, this is a multi-period, piece-wise linear dynamic optimisation problem. The key result of this optimization problem is illustrated in Figure 29 below.



**Figure 29.** Exhaust gas venting. In this scenario, approximately 23% of the exhaust gas was vented during periods of peak electricity prices.

As can be observed from Figure 29, during periods of peak electricity prices, approximately 23% of the total exhaust gas was vented. In this scenario, we departed from the conventional procedure of capturing 90% of the CO<sub>2</sub> at all times. Rather, of the exhaust gas which was introduced into the absorption column, 95 % of the CO<sub>2</sub> was captured. However, during the periods of exhaust gas venting, the DoC fell to approximately 74 %, increasing the carbon intensity of the electricity generated to approximately 225 kg/MWh. This is illustrated in Figure 30. It is noted that the venting of this quantity of CO<sub>2</sub> had the primary consequence of imposing a significant cost penalty on the profitability of the plant and the secondary consequence that it was not possible to solve the optimization problem with the end-point constraint of IDoC ≥ 90 %. Here, this had to be loosened to 89 %.



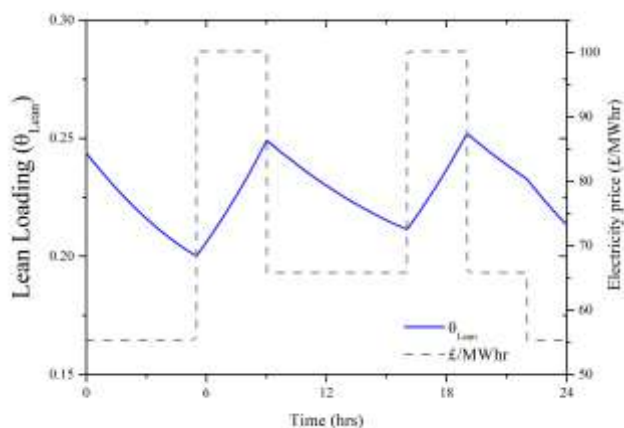
**Figure 30.** Variation in DoC with exhaust gas venting. It can be observed here that the absorber DoC remains approximately constant.

### Time-varying solvent regeneration

In this section, we evaluate the option of using the working solvent as means to provide flexibility to the power plant. This is achieved by allowing the CO<sub>2</sub> to accumulate in the working solvent during hours of peak electricity prices and regenerating the solvent more completely during off peak periods. This is not storing solvent separately to the capture plant; this is storing CO<sub>2</sub> in the solvent which is circulating within the capture plant. This means that the lean loading of the solvent is no longer a time-invariant process parameter. Rather, this control vector is now parameterised such that it is expressed as:

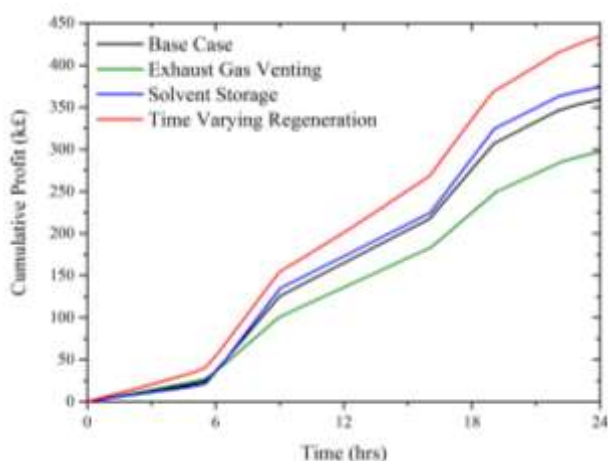
$$\theta_{Lean}^k = \alpha^k t^2 + \beta^k t + \gamma^k \quad (5)$$

where  $\theta_{Lean}^k$  is the function describing the way in which  $\theta_{Lean}$  varies across a given period  $k$ ,  $\alpha^k$ ,  $\beta^k$  and  $\gamma^k$  describe this function in each period  $k$  and finally  $t$  is the time in each period  $k$ . Here, the variable  $t$  is set to zero at the beginning of each new period. The only additional constraint we have imposed upon the optimisation problem by this formulation is the quadratic nature of the parameterisation. This could have equally been a cubic or higher order polynomial, however a quadratic polynomial was chosen in the interest of simplicity. Further, we did not constrain the values of the coefficients of this polynomial, i.e., the magnitude of the subsequent behaviour was strictly a function of the process response to the time-varying electricity prices. The results of this optimisation problem are presented in Figure 31.



**Figure 31.** Solvent regeneration as a function of time and electricity price is shown here.

As can be observed, and as opposed to operating at a constant lean loading (the continuous blue curve), the degree of solvent regeneration varies in sympathy with the prevailing electricity price, as might be expected for the solution of this kind of optimisation problem. The solvent is deeply regenerated during periods of low electricity price, whilst CO<sub>2</sub> is allowed to accumulate in the working solvent volume during periods of high electricity price. This has the effect of allowing the plant to direct substantially less steam to solvent regeneration operations when the opportunity cost associated with doing so is high. Obviously, following this kind of operating strategy will have the effect of varying the carbon intensity of the electricity generated.



**Figure 32.** Cumulative profit available for each option.

It is finally instructive to consider the profitability of the power plant, which is illustrated in Figure 32. It is apparent that the solvent storage option offers marginally greater profitability (circa

£374k) when compared with the base case (circa £359.6k), approximately a 4 % improvement, whereas the exhaust gas venting option (circa £298.6k) is approximately 17 % less profitable than the base case. Finally, the variable solvent regeneration option (£417.5k) is 16 % more profitable than the base case scenario.



## Development of Near-field Dispersion Model

**R.M. Woolley, M. Fairweather, and S.A.E.G. Falle**

*University of Leeds, UK*

Following the puncture or rupture of a CO<sub>2</sub> pipeline, a gas-liquid droplet mixture or gas alone will be released to atmosphere and disperse over large distances. This may be then followed by gas-solid discharge during the latter stages of pipeline depressurisation due to the significant degree of cooling taking place. The possibility of releases of three-phase mixtures also exists. This paper focuses on the detailed mathematical modelling of the near-field characteristics of these complex releases, since predictions of major hazards used in risk assessments are based on the use of near-field source terms that provide input to far-field dispersion models.

Because the pre- to post-expansion pressure ratio resulting from a release will initially be large, the sonic velocity will be reached at the outlet of the pipeline and the resulting free jet will be sonic. This pressure difference leads to a complex shock cell structure within the jet which for the initial highly under-expanded flow will give rise to a flow that contains a Mach disk followed by a series of shock diamonds as it gradually adjusts to ambient conditions. Subsequently, consideration has to be made to the complex physics representing the effects of compressibility upon turbulence generation and destruction. Also, the behaviour of a multi-phase non-ideal system has to be represented by the incorporation of a non-ideal equation of state to represent mass-transfer between phases at a range of temperatures and pressures.

### Turbulent flow modelling

Descriptions of the numerical approaches to the solution of the fluid dynamics equations applied are presented elsewhere [28], and not repeated here. Also, the last newsletter discussed the application of modified two-equation turbulence models to represent a compressible system, which shall not be revisited. With respect to two-

equation turbulence modelling however, It is now widely accepted that the main contributor to the structural compressibility effects is the pressure-strain term ( $\Pi_{ij}$ ) appearing in the transported Reynolds stress equations [29]. Hence, the use of compressible dissipation models is now considered physically inaccurate, although their performance is good.

Ignoring the rapid part of the pressure-strain correlation, Rotta [30] models the term as Equation (6) where  $\varepsilon$  is the dissipation of turbulence kinetic energy, and  $b_{ij}$  is the Reynolds stress anisotropy, as defined in the first term of Equation (3) below:

$$\Pi_{ij} = -C_1 \varepsilon b_{ij} \quad (6)$$

Later, this model was extended [31] to directly incorporate terms arising from compressibility effects as Equation (7):

$$\Pi_{ij} = -C_1 (1 - \beta M_t^2) \varepsilon b_{ij} \quad (7)$$

where  $\beta M_t$  is a function of the turbulent Mach number, vanishing in an incompressible flow.

Prior to this development, Jones and Musonge [32] provide a model to account for the 'rapid' element of the correlation. Defining a function for the fourth-rank linear tensor in the strain-containing term with the necessary symmetry properties, they obtain:

$$\begin{aligned} \Pi_{ij} = & -C_1 \varepsilon \left( \frac{\bar{\rho} u_i'' u_j''}{k} - \frac{2}{3} \delta_{ij} \bar{\rho} \right) + C_2 \delta_{ij} \bar{\rho} u_i'' u_j'' \frac{\partial \tilde{u}_k}{\partial x_l} \\ & - C_3 P_{ij} + C_4 \bar{\rho} k \left( \frac{\partial \tilde{u}_i}{\partial x_j} + \frac{\partial \tilde{u}_j}{\partial x_i} \right) + C_5 \bar{\rho} u_i'' u_j'' \frac{\partial \tilde{u}_l}{\partial x_l} \\ & + C_6 \left( \bar{\rho} u_k'' u_j'' \frac{\partial}{\partial x_k} (\tilde{u}_k) + \bar{\rho} u_k'' u_i'' \frac{\partial}{\partial x_j} (\tilde{u}_k) \right) \\ & + C_7 \bar{\rho} k \delta_{ij} \frac{\partial \tilde{u}_l}{\partial x_l} \end{aligned} \quad (8)$$

where the  $C_1$  term corresponds to the 'slow' part as previously defined as Equation (6),  $k$  is

the turbulence kinetic energy,  $\bar{\rho}$  the mean density,  $\delta_{ij}$  the Kroncker delta, and  $u''u''$  and  $\tilde{u}$  the Favre-averaged Reynolds stresses and velocity components, respectively.

Defining the gradient and turbulent Mach numbers as:

$$M_g \equiv \frac{Sl}{a} \quad \text{and} \quad M_t \equiv \frac{\sqrt{2k}}{a} \quad (9)$$

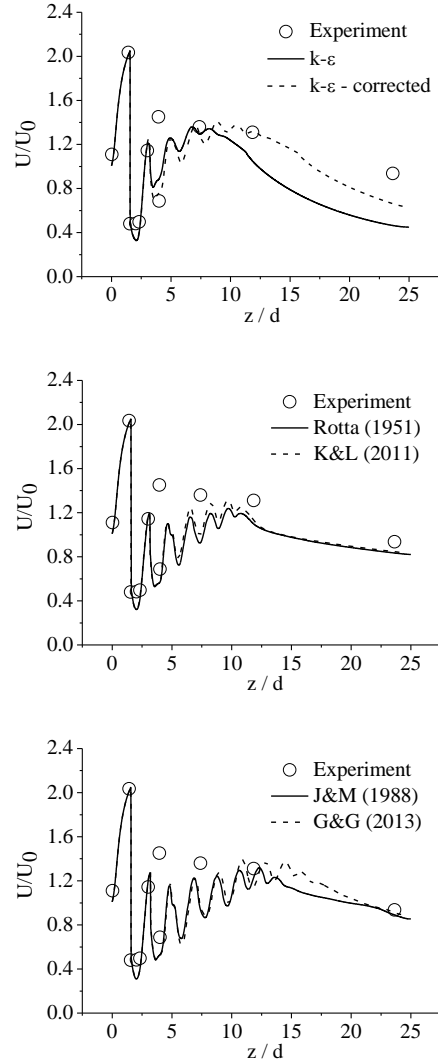
Gomez and Girimaji [33] introduce corrections to their derivation of  $\Pi_{ij}$  as Equation (5), which is implemented in terms of a modification to Equation (8) in the current work:

$$\Pi_{ij} = -C_1(M_t)b_{ij} + \sum_k C_k(M_g)T_{ij}^k \quad (10)$$

The turbulent Mach number is the ratio of the magnitude of the velocity fluctuations to the speed of sound, and the dependence of the 'slow' part reflects the degree of influence of dilatational fluctuations. The gradient Mach number characterises the shear to acoustic time scales, and its influence upon the 'rapid' part corresponds to the fluctuating pressure field which arises due to the presence of the mean velocity gradient.

Figure 33 depicts the application of these turbulence closures to the prediction of centreline axial velocity, normalised by the magnitude at the nozzle exit, for the highly under-expanded air jet studied by Donaldson and Snedeker [34]. Results obtained using the  $k-\epsilon$  model and its associated correction attributed to Sarkar, Erlebacher [35] can be seen to conform with observations previously made with respect to the moderately under-expanded air jet. In this case, the initial shock structure is poorly defined by the standard model, and the over-predicted dissipation of these phenomena is considerable by ten nozzle diameters from the jet outflow. The Sarkar modification to the turbulence dissipation goes some way to reducing the over-prediction up to approximately 15 diameters, but the resolution of the initial shock-laden region remains poor, and the solution subsequently becomes overly dissipative.

The Reynolds stress transport model with the closure of the pressure-strain correlation attributed to Rotta [30] notably improves upon the resolution of the shock region and the prediction of the dissipation of turbulence kinetic



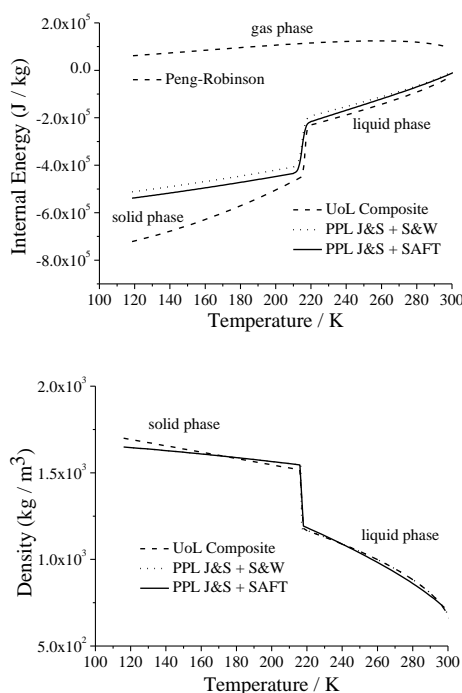
**Figure 33.** Normalised velocity predictions (top –  $k-\epsilon$ , middle and bottom – Reynolds stress) plotted against experiment.

energy. The introduction of a compressible element to the 'slow' part of the model as discussed by Khlifi and Lili [31] effects an additional increase in peak magnitude predictions in the near field, although has little effect upon the subsequent downstream turbulence dissipation. The application of a model for the 'rapid' part of the pressure-strain term [32], incorporated with the simple model of Rotta for the 'slow' part proves a significant improvement with respect to predictions of both the shock resolution and the turbulence dissipation. This is again improved upon by the introduction of corrections based upon the turbulent and gradient Mach numbers as outlined by Gomez and Girimaji [33].

## Thermodynamics modelling

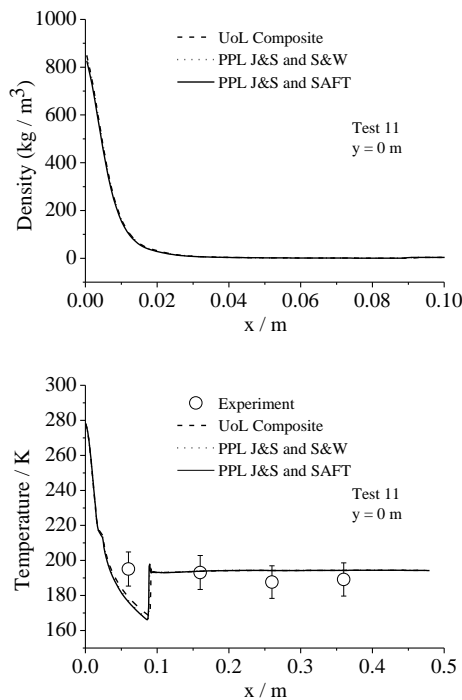
The Peng-Robinson [36] equation of state is satisfactory for modelling the gas phase, but when compared to that of Span and Wagner [37], it is not so for the condensed phase, as demonstrated by Wareing, Woolley [38]. Furthermore, it is not accurate for the gas pressure below the triple point and, in common with any single equation, it does not account for the discontinuity in properties at the triple point. In particular, there is no latent heat of fusion. A number of composite equations of state have therefore been constructed by the authors for the purpose of comparing performance in application to practical problems of engineering interest. In these, the gas phase is computed from the Peng-Robinson equation of state, and the liquid phase and saturation pressure are calculated from tabulated data generated with the Span and Wagner equation of state, or from an advanced model based upon statistical associating fluid theory (SAFT) [7]. Solid phase properties are obtained from an available source of thermodynamic data for CO<sub>2</sub>, the Design Institute for Physical Properties (DIPPR) 801 database (<http://www.aiche.org/dippr>), or from a recently developed model attributed to Jager and Span [39].

Under the remit of the CO<sub>2</sub>QUEST FP7 project, the development of a Physical Properties Library (PPL), and hence the provision of a 'platform' capable of predicting physical and thermodynamic properties of pure CO<sub>2</sub> and its mixtures, has been undertaken. The PPL contains a collection of models which can be applied regardless of the application, and include a number of cubic formulations such as those described by Peng and Robinson, and Soave, and the formulation of Span and Wagner. Also available is the analytical equation of Yokozeki [40], and the advanced molecular models described as SAFT and PC-SAFT by Gross and Sadowski [9]. A comparative study of the performance of these equations of state has been undertaken using experimental data of high-pressure CO<sub>2</sub> releases for validation. Due to space restrictions, a representative sample of these results is presented which include the composite model described above, and the PPL-derived Jager and Span [39] model coupled with both Span and Wagner [37] and SAFT. Figure 34 depicts density and internal energy predictions for both the condensed and the gaseous phases on the saturation line for a pure CO<sub>2</sub> system obtained using these three different approaches. Importantly, it can be seen that all models incorporate the latent heat of fusion which must be considered over the liquid-solid phase boundary. They can also be said to similarly represent the internal energy of the liquid phase, although a discrepancy is observed with the composite model. This can be attributed to the inclusion in that model of a small value to ensure conformity with Span and Wagner [37] in terms of the predicted difference between gas and liquid energies [38]. The major discrepancy in predictions lies in the solid-phase region, in that the composite model is in notable disagreement with the models incorporating Jager and Span [39]. This can be attributed to the sources of experimental data used in the derivation of the respective models, and the reader is referred to these papers for further information regarding the data sources.



**Figure 34.** Saturation-line internal energy and density predictions of pure CO<sub>2</sub> using three different equations of state compositions.

## Validation against experimental CO<sub>2</sub> releases



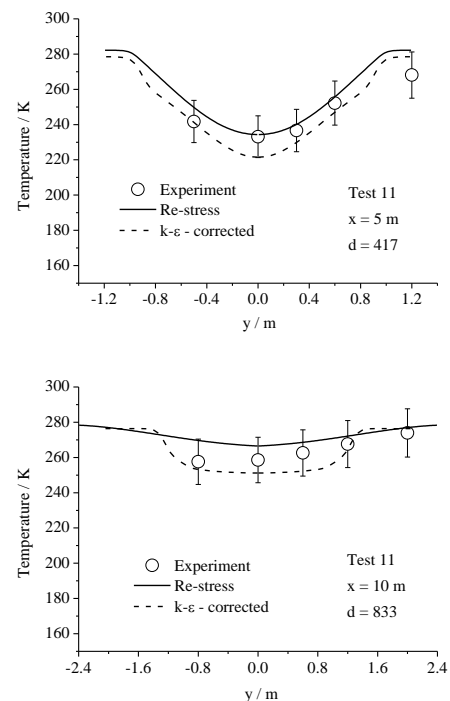
**Figure 35.** Mean density and temperature predictions of a large scale, sonic release of CO<sub>2</sub> plotted against experimental data.

Figure 35 presents sample density and temperature predictions of one of the large-scale test cases used for the validation of the code, obtained using the second-moment turbulence closure [33] and three of the composite equations of state. Undertaken by INERIS, the experimental parameters were a reservoir pressure of 83 bar, an exit nozzle diameter of  $12.0 \times 10^{-3}$  m, and an observed mass flow rate of  $7.7 \text{ kg s}^{-1}$ . The predictions are of the very near field of the jet, encompassing the nozzle exit, and in the case of the temperature, extending to 0.5 metres downstream. This equates to a distance of approximately 42 nozzle diameters ( $d$ ), and the Mach disc can clearly be seen as a step-change in temperature just before 0.1 metres. Temperature predictions are in good quantitative agreement with experimental data within this region, although it is difficult to assess how the model performs qualitatively due to the resolution of the temperature measurements available. The difference in predicted solid-phase properties can be seen to influence the temperature predictions most notably in the region 0.02 metres to 0.1 m, where the composite model predicts a warmer

jet. Not unexpectedly, this region coincides with the system passing through the triple point at 216.5 K, being notable by the small step-change in the temperature curve of Figure 35, and the subsequent freezing of the liquid CO<sub>2</sub>.

Density predictions derived from the three models appear to be in good agreement within the very near-field, although closer scrutiny of the predictions reveals the effect of the different solid-phase models. Contrary to intuition, the composite equation predicts a slightly higher density in the first 0.03 metres, but conversely predicts a slightly higher temperature in the region bounded by the triple point and the stationary shock. It is considered that this observation is due to two factors. Initially, the predicted density of the liquid release obtained from this model is greater due to the observed differences in the liquid-phase predictions (Figure 34). Subsequently, as the system passes through the triple point, the composite model predicts slightly higher temperatures for the solid-phase, which relates to a small correction in the density, bringing them in to line with the PPL-derived models.

Further downstream, and with reference to Figure 36, predictions obtained using the Reynolds-stress model of Gomez and Girimaji [33] and the composite equation of state, are



**Figure 36.** Mean temperature predictions within a large scale, sonic release of CO<sub>2</sub> plotted against experimental data.



conforming with experimental data both qualitatively and quantitatively, although a slight over-prediction of temperature can be seen across the width of the jet and also with downstream progression. This is indicative of a marginally over-predicted rate of mixing, in-line with previous observations made of the turbulence model validations. It can be said that the second-moment model out-performs the  $k-\epsilon$  approach when coupled with the composite equation of state, in that the rate of mixing is better represented. This is manifest as a notable under-prediction of temperatures along the jet axis and also across its width, where the shear layer of the jet is observable as a temperature change of steep gradient, not observed in the Reynolds stress predictions.

Presented are sample results from a number of turbulence and thermodynamics models which have been developed to accurately predict the flow structure and phase behaviour of accidental releases of high-pressure  $\text{CO}_2$  for engineering applications. An excellent level of agreement between modelling approaches and experimental data has been observed.

## **The impact of impurities on storage**

**J. Bensabat and R. Segev**

*EWRE Ltd., Haifa, Israel*

EWRE work has focused on the configuration of the field experiment aimed at investigating the impact of impurities upon the storage of  $\text{CO}_2$ . Firstly, we have reviewed major likely impurities emitted with  $\text{CO}_2$  from the capture systems, and it was suggested to use one with a potential geochemical impact ( $\text{SO}_2$ ) and one with potential physical impact ( $\text{N}_2$ ). Simulations of the behaviour of these impurities upon the reservoir were conducted in order to determine suitable mass fractions that induce a detectable change in the reservoir response. Once the impurities and the mass fractions are known we will then proceed to the preparations of the experiment in the field, and the actual procedure for the injection of the impurities with the  $\text{CO}_2$ . We have reviewed three options: 1) purchasing a prepared mixture of  $\text{CO}_2$ ,  $\text{N}_2$ , and  $\text{SO}_2$ , that could be injected directly; 2) conducting the mixing at the wellhead of the injection well; and 3) conducting the mixing at a depth of approximately 1,000 m, as the injection well has an independent connection from the ground surface to this depth.

The field experiment will take place at Heletz (Israel), where two deep wells (1650 m) fully instrumented for monitoring down-hole pressure and temperature, continuous temperature sensing via optical fiber, fluid sampling, fluid abstraction, and  $\text{CO}_2$  injection. Design and procurement (or rental) of the equipment needed for the injection of the impurities is currently under way.

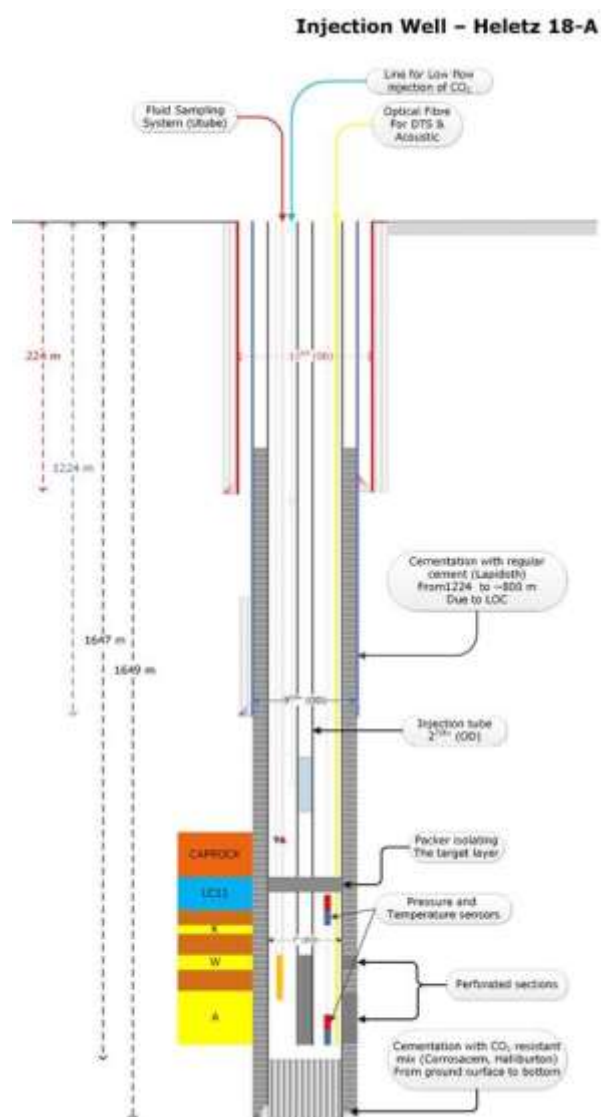
The experiment is planned for the first quarter of 2015.



**Figure 37.** Aerial photograph of the site (and the wells)



**Figure 39.** Injection module – 1



**Figure 38.** Structure of the injection well



**Figure 40.** Injection module – heat exchanger


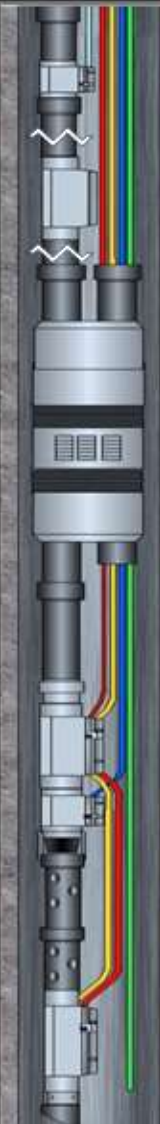
							
Company: Class 6 Solutions Heletz Mon		Date: 27-Jan-14	Temp: 130 °F	Gun Size: 0"	SPF: 0	Phasing: 0°	Casing Size/Wt: 7
Well Name: H18 Injection	Field: 0	Expl. Type: 0	Fluid Wt: 8.5#	Fluid Type: 2% KCL	Job Type: Horizontal TCP		
County/Parish: 0	State: 0	Completion Intervals: VI	Firing Device #1: 0		Firing Device #2: 0		
Item	Description	O. D.	I. D.	Length	Depth Feet	Depth Meters	
	Run 162 total joints and 1 perf joint						
24	Tubing to Surface	3.660	2.441	2,929.55	-	-	
23	Chemical Injection Sub	3.660	2.441	4.09	2,929.55	892.93	
22	10 Joints 2 7/8" Pipe Joint 63-72	3.660	2.441	325.73	2,933.64	894.17	
21	Gas Lift Mandrel	3.660	2.441	4.09	3,259.37	993.46	
20	58 Joints 2 7/8" Pipe Joints 4-62	3.660	2.441	1,922.02	3,263.46	994.70	
19	Marker Sub	3.660	2.441	6.30	5,185.48	1,580.53	
18	1 Joint 2 7/8" Tubing #3	3.660	2.441	32.57	5,191.78	1,582.45	
17	X-Nipple	3.660	1.875	0.99	5,224.35	1,592.38	
16	1 Joint 2 7/8" Tubing #2	3.660	2.441	32.59	5,225.34	1,592.68	
15	7" 23# Dual String Packer	6.062	2.441	7.83	5,257.93	1,602.62	
14	1 Joint 2 7/8" Tubing #1	3.660	2.441	32.58	5,265.76	1,605.00	
13	On/Off Tool w/ X profile	4.500	1.875	1.85	5,298.34	1,614.93	
12	X-O Pup	3.660	2.441	6.09	5,300.19	1,615.50	
11	Dual Gauge Carrier	4.850	2.441	5.67	5,306.28	1,617.35	
10	Sample Filter Carrier	3.990	2.441	3.00	5,311.95	1,619.08	
9	X-O 2 7/8" NU Box X 2 3/8" Pin	3.660	2.100	0.40	5,314.95	1,620.00	
8	Pump out plug	3.063	1.875	0.68	5,315.35	1,620.12	
7	X-O 2 3/8" Box X 2 7/8" Pin and 2' pup	3.660	1.995	2.67	5,316.03	1,620.33	
6	1 Joint 2 7/8" Perforated Pipe	3.660	2.441	32.55	5,318.70	1,621.14	
5	X-O Pup	3.660	2.441	6.08	5,351.25	1,631.06	
4	Dual Gauge Carrier	4.850	2.441	5.67	5,357.33	1,632.91	
3	X-O Pup and Fiber Termination Sub	3.660	2.441	5.62	5,363.00	1,634.64	
2	Wireline Re-entry Guide and XN Nipple	3.660	2.441	1.38	5,368.62	1,636.36	
1	Bottom of W/L Re-entry Guide				5,370.00	1,636.78	
Comments: Perforations:				Total Length of BHA =	2440.45'	743.85'	
				Total BHA w/o Pipe =	94.96	28.94	

Figure 41. Injection well (as made)

## Industrial scale pipeline for CO<sub>2</sub> release experiments

**S. Chen and Y. Zhang**

*School of Chemical Engineering, Dalian University of Technology, China*

Three pure CO<sub>2</sub> release experiments, including one full bore rupture release, have been undertaken using the relocated industrial-scale pipeline in Dalian, China. Impure CO<sub>2</sub> release experiments were also performed in October 2014.

The fully instrumented pipeline is 256m long with a 233mm inner diameter, and CO<sub>2</sub> temperature measurements were obtained at numerous points in the near field.

The following figures show the release facility and the full bore rupture results.

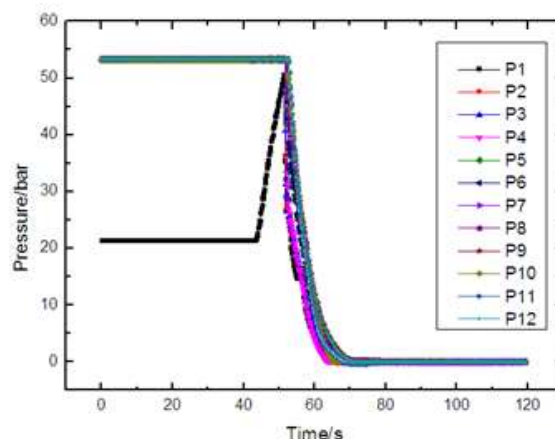


**Figure 42.** CO<sub>2</sub> release experimental facility in Dalian, China.

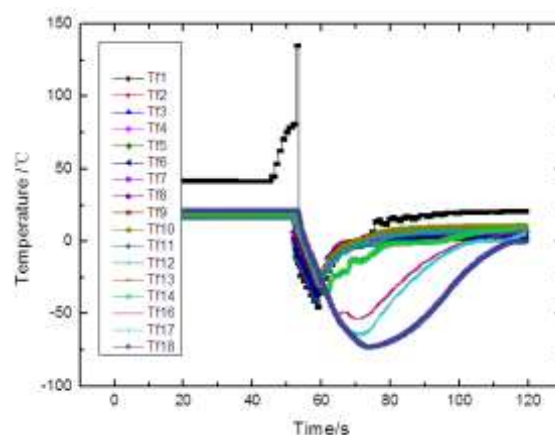


**Figure 43.** Full-bore rupture release stills with an inventory of 2.43 tonnes pure CO<sub>2</sub> under the following conditions: ambient temperature 36° C, pipeline

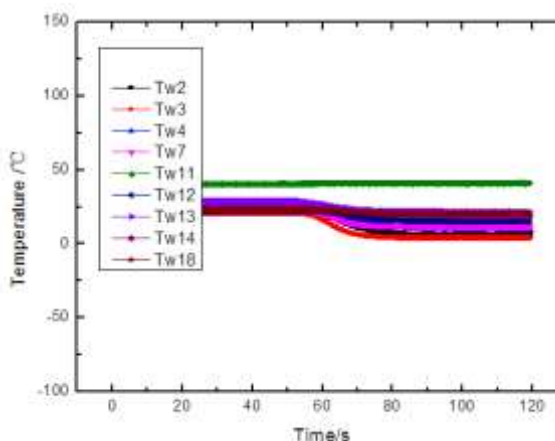
pressure 52.5 bar, humidity 59 % and CO<sub>2</sub> temperature in the pipeline of 20~30° C.



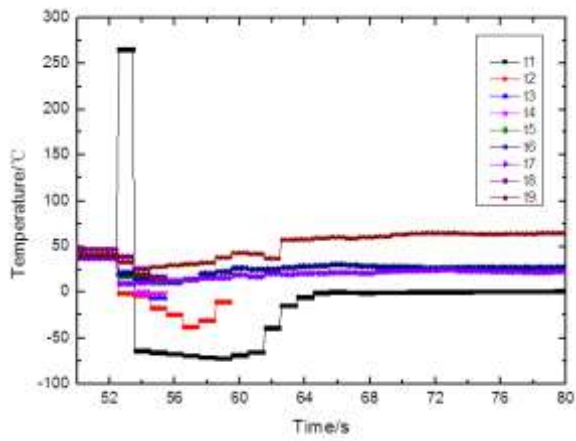
**Figure 44.** Pressure drop within the pipeline during the full bore rupture release. P1 (release end) to P12 (closed end).



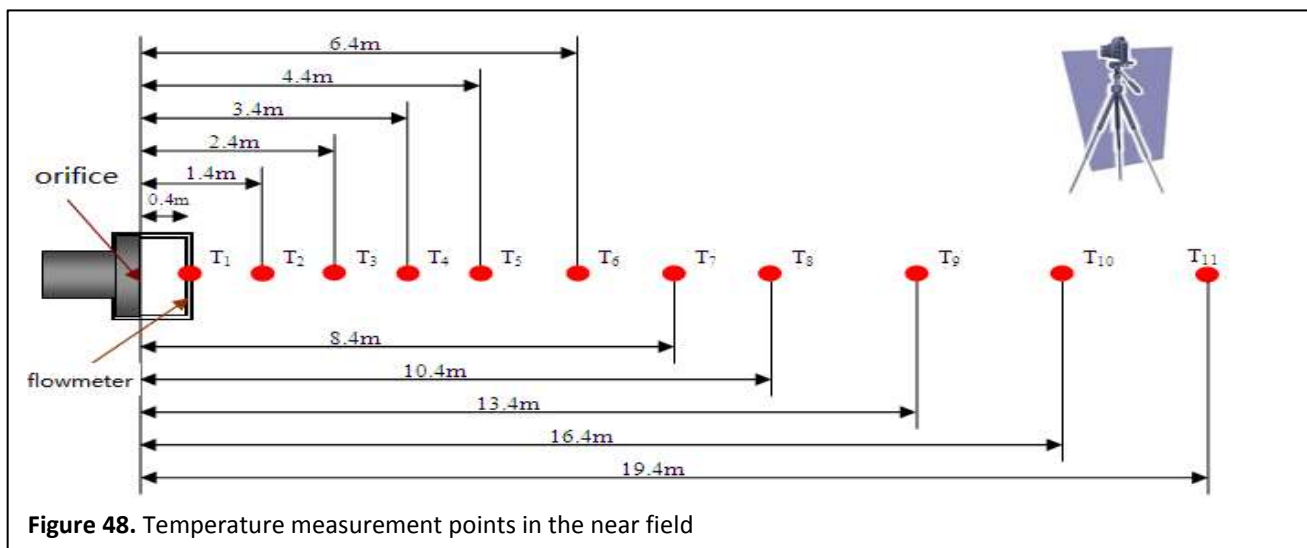
**Figure 45.** Temperature change along the pipeline during the full-bore release.



**Figure 46.** Temperature change of the pipeline wall during the full-bore release.



**Figure 47.** Temperature change in the release near-field during the full-bore release.



**Figure 48.** Temperature measurement points in the near field



# International Forum on Recent Developments of CCS Implementation

Leading the way to a low-carbon future

**CONFIRMED  
SPEAKERS &  
CALL FOR  
ABSTRACTS**

Co-organised by

**CO<sub>2</sub>QUEST**

**IoLiCAP**

ECR funding is available  
from



**26th —27th  
MARCH 2015**

## Confirmed Speakers

The organising committee are delighted to announce the following keynote speakers:



Dr. Vassilios Kougionas - DG Research & Innovation, European Commission - **"Future EC Funding Strategy and Opportunities in CCS"**

Mr. John Gale- General Manager, IEA Greenhouse Gas R&D Programme - **"A Global Overview of CCS Implementation"**



Dr. Paul Fennel - Reader in Clean Energy, Imperial College London - **"Comparative Costings for 1st, 2nd and 3rd Generation CCS technologies"**

Mr. Russell Cooper - Technical Services Manager, National Grid, UK - **"The White Rose CCS Project"**



## Call for Abstracts

Abstracts called for the following sessions:

- |   |   |                           |
|---|---|---------------------------|
| Whole-systems CCS                             | Bioenergy with CCS, and Carbon Neutral Technologies |                           |
| CCS for CO <sub>2</sub> -intensive Industries | Demonstration Projects                              |                           |
| CO <sub>2</sub> Capture                       | CO <sub>2</sub> Storage                             | CO <sub>2</sub> Transport |
| Materials for CCS                             | Governance of Development and Deployment of CCS     |                           |

Both academic and industrial contributions will be represented at the meeting. An abstract template can be found on the event website.

With contributions from  
leading FP-7 EC Projects

**CO<sub>2</sub>QUEST**

**IoLiCAP**

**IMPACTS**

## VENUE

Athens Ledra Hotel, 115 Syngrou Avenue, Athens, Greece

## REGISTRATION DEADLINE

Early bird registration (only € 440 including accommodation) is available until the

**31st January 2015.**

## CALL FOR ABSTRACTS

We invite you to submit an abstract for either oral or poster presentation.

Deadline for submissions is the **15th December 2015.**

**FOR MORE INFORMATION,  
PLEASE VISIT THE EVENT  
WEBSITE:**

<http://goo.gl/3wjUDH>



To register <http://goo.gl/xkMVcq>  
contact Abigail Ward: [A.M.E.Ward@leeds.ac.uk](mailto:A.M.E.Ward@leeds.ac.uk)



## Publications and Conference Participation

News regarding the up-coming CO2QUEST technical workshop will be posted on the website.

<http://www.co2quest.eu/>

A number of papers, posters, and presentations are also available in the publications section of the project website. For regular updates on publications please visit:

<http://www.co2quest.eu/publications.htm>

## Acknowledgement and Disclaimer

The authors gratefully acknowledge funding received from the European Union 7<sup>th</sup> Framework Programme FP7-ENERGY-2009-1 under grant agreement number 241346.

The newsletter reflects only the authors' views and the European Union is not liable for any use that may be made of the information contained therein.

## References

1. Moore, J.J., Allison, T., Lerche, A., Pacheco, J., and Delgado, H. *Development of Advanced Centrifugal Compressors and Pumps for Carbon Capture and Sequestration Applications*. in *The Fortieth Turbomachinery Symposium* 2011, Houston, Texas 107-120.
2. Witkowski, A. and Majkut, M., *The Impact of CO<sub>2</sub> Compression Systems on the Compressor Power Required for a Pulverized Coal-fired Power Plant in Post-combustion Carbon Dioxide Sequestration*. **The Archive of Mechanical Engineering**, 2012. 59(3).
3. Martynov, S. and Brown, S., *CO2QUEST Internal Report: A Report Describing the Optimum CO<sub>2</sub> Compression Strategy*. Deliverable 2.2, University College London, UK. 2014.
4. Mahgerefteh, H., Denton, G., and Rykov, Y., *A Hybrid Multiphase Flow Model*. **AIChE Journal**, 2008. 54(9): 2261-2268.
5. Mahgerefteh, H., Oke, A., and Atti, O., *Modelling Outflow Following Rupture in Pipeline Networks*. **Chemical Engineering Science**, 2006. 61(6): 1811-1818.
6. Diamantonis, N.I. and Economou, I.G., *Evaluation of Statistical Associating Fluid Theory (SAFT) and Perturbed Chain-SAFT Equations of State for the Calculation of Thermodynamic Derivative Properties of Fluids Related to Carbon Capture and Sequestration*. **Energy & Fuels**, 2011. 25(7): 3334-3343.
7. Diamantonis, N.I., Boulougouris, G.C., Mansoor, E., Tsangaris, D.M., and Economou, I.G., *Evaluation of Cubic, SAFT, and PC-SAFT Equations of State for the Vapor-liquid Equilibrium Modeling of CO<sub>2</sub> Mixtures with other Gases*. **Industrial and Engineering Chemistry Research**, 2013. 52(10): 3933-3942.
8. Diamantonis, N.I., Boulougouris, G.C., Tsangaris, D.M., Kadi, M.J.E., Saadawi, H., Negaban, S., and Economou, I.G., *Thermodynamic and Transport Property Models for Carbon Capture and Sequestration (CCS) Processes with Emphasis on CO<sub>2</sub> Transport*. **Chemical Engineering Research and Design**, 2013. 91: 1793-1806.
9. Gross, J. and Sadowski, G., *Perturbed-Chain SAFT: An Equation of State Based on a Perturbation Theory for Chain Molecules*. **Industrial and Engineering Chemistry Research**, 2001. 40(4): 1244-1260.
10. Diamantonis, N.I. and Economou, I.G., *Modeling the Phase Equilibria of a H<sub>2</sub>O-CO<sub>2</sub> Mixture with PC-SAFT and tPC-PSAFT Equations of State*. **Molecular Physics**, 2012. 110: 1205-1212.
11. NIST. *NIST Chemistry WebBook*, 2014. Accessed 10/11/14; Available from: <http://webbook.nist.gov>.
12. Potter, R.W. and Brown, D.L., *The Volumetric Properties of Aqueous Sodium Chloride Solutions from 0° to 50°C at Pressures up to 2000 Bars Based on a Regression of Available Data in the*

- Literature. Bulletin 1421-C, United States Geological Survey: Washington. 1977.
13. Yan, W., Huang, S., and Stenby, E.H., *Measurement and Modeling of CO<sub>2</sub> Solubility in NaCl Brine and CO<sub>2</sub> Saturated NaCl Brine Density*. **International Journal of Greenhouse Gas Control**, 2011. 5: 1460-1477.
14. Jiang, H. and Adidharma, H., *Study of Thermodynamic Properties of Symmetric and Asymmetric Electrolyte Systems in Mixture with Neutral Components: Monte Carlo Simulation Results and Integral Equation Predictions*. **Molecular Simulation**, 2014: In press.
15. CO2PipeHaz. *Quantitative Failure Consequence Hazard Assessment for Next Generation CO<sub>2</sub> Pipelines: The Missing Link*, 2009. Accessed 11/11/14; [CO2PipeHaz Project Website]. Available from: <http://www.co2pipehaz.eu/>.
16. Jamois, D., Proust, C., and Hebrard, J., *Hardware and Instrumentation to Investigate Massive Spills of Dense Phase CO<sub>2</sub>*. **Chemical Engineering Transactions**, 2014. 36: 601-606.
17. Martynov, S., Brown, S., Mahgerefteh, H., Sundra, V., Chen, S., and Zhang, Y., *Modelling Three-phase Releases of Carbon Dioxide from High-pressure Pipelines*. **Journal of Process Safety and Environmental Protection**, 2013. 92(1): 36-46.
18. Grossmann, I.E. and Sargent, R.W.H., *Optimum design of multipurpose chemical plants*. **Industrial and Engineering Chemistry Process Design and Development**, 1979. 18(2): 343-348.
19. Arce, A., Mac Dowell, N., Shah, N., and Vega, L.F., *Flexible operation of solvent regeneration systems for CO<sub>2</sub> capture processes using advanced control techniques: Towards operational cost minimisation*. **International Journal of Greenhouse Gas Control**, 2012. 11: 236-250.
20. Mac Dowell, N. *Optimisation of post-combustion CCS for flexible operation*. in *The 14th Annual APGTF Workshop - 'The Role of Fossil Fuel Power Plant in Providing Flexible Generation'* 2014, London.
21. Mac Dowell, N., Galindo, A., Jackson, G., and Adjiman, C.S., *Integrated solvent and process design for the reactive separation of CO<sub>2</sub> from flue gas*. **Computer Aided Chemical Engineering**, 2010. 28: 1231-1236.
22. Mac Dowell, N., Pereira, F.E., Llovel, F., Blas, F.J., Adjiman, C.S., Jackson, G., and Galindo, A., *Transferable SAFT-VR models for the calculation of the fluid phase equilibria in reactive mixtures of carbon dioxide, water, and n-alkylamines in the context of carbon capture*. **Journal of Physical Chemistry B**, 2011. 115(25): 8155-8168.
23. Mac Dowell, N., Samsatli, N.J., and Shah, N., *Dynamic modelling and analysis of an amine-based post-combustion CO<sub>2</sub> capture absorption column*. **International Journal of Greenhouse Gas Control**, 2013. 12: 247-258.
24. Mac Dowell, N. and Shah, N., *Dynamic modelling and analysis of a coal-fired power plant integrated with a novel split-flow configuration post-combustion CO<sub>2</sub> capture process*. **International Journal of Greenhouse Gas Control**, 2014. 27: 103-119.
25. Mac Dowell, N. and Shah, N., *The multi-period operation of an amine-based CO<sub>2</sub> capture process integrated with a supercritical coal-fired power station*. **Computers and Chemical Engineering**, 2014 (Under Review).
26. Rodriguez, J., Mac Dowell, N., Llovel, F., Adjiman, C.S., Jackson, G., and Galindo, A., *Modelling the fluid phase behaviour of aqueous mixtures of multifunctional alkanolamines and carbon dioxide using transferable parameters with the SAFT-VR approach*. **Molecular Physics**, 2012. 110(11-12): 1325-1348.
27. Mac Dowell, N. and Shah, N., *Identification of the cost-optimal degree of CO<sub>2</sub> capture: An optimisation study using dynamic process models*. **International Journal of Greenhouse Gas Control**, 2013. 13: 44-58.
28. Woolley, R.M., Fairweather, M., Wareing, C.J., Falle, S.A.E.G., Proust, C., Hebrard, J., and Jamois, D., *Experimental Measurement and Reynolds-Averaged Navier-Stokes Modelling of the Near-Field*



- Structure of Multi-phase CO<sub>2</sub> Jet Releases. International Journal of Greenhouse Gas Control*, 2013. 18(1): 139-149.
29. Sarkar, S., *The Stabilizing Effect of Compressibility in Turbulent Shear Flow. Journal of Fluid Mechanics*, 1995. 282: 163-186.
  30. Rotta, J., *Statistische Theorie nichthomogener Turbulenz. 1. Mitteilung. Zeitschrift für Physik A-Hadrons and Nuclei*, 1951. 129: 547-572.
  31. Khelifi, H. and Lili, T., *A Reynolds Stress Closure for Compressible Turbulent Flow. Journal of Applied Fluid Mechanics*, 2011. 4(2): 99-104.
  32. Jones, W.P. and Musonge, P., *Closure of the Reynolds Stress and Scalar Flux Equations. Physics of Fluids*, 1988. 31(12): 3589-3604.
  33. Gomez, C.A. and Girimaji, S.S., *Toward Second-moment Closure Modelling of Compressible Shear Flows. Journal of Fluid Mechanics*, 2013. 733: 325-369.
  34. Donaldson, C.D. and Snedeker, R.S., *A Study of Free Jet Impingement. Part 1. Mean Properties of Free and Impinging Jets. Journal of Fluid Mechanics*, 1971. 45(2): 281-319.
  35. Sarkar, S., Erlebacher, G., Hussaini, M.Y., and Kreiss, H.O., *The Analysis and Modelling of Dilatational Terms in Compressible Turbulence. Journal of Fluid Mechanics*, 1991. 227(1): 473-493.
  36. Peng, D.-Y. and Robinson, D.B., *A New Two-Constant Equation of State. Industrial and Engineering Chemistry Fundamentals*, 1976. 15(1): 59-64.
  37. Span, R. and Wagner, W., *A New Equation of State for Carbon Dioxide Covering the Fluid Region from the Triple-Point Temperature to 1100 K at Pressures up to 800 MPa. Journal of Physical and Chemical Reference Data*, 1996. 25(6): 1509-1596.
  38. Wareing, C.J., Woolley, R.M., Fairweather, M., and Falle, S.A.E.G., *A Composite Equation of State for the Modelling of Sonic Carbon Dioxide Jets. American Institute of Chemical Engineers Journal*, 2013. 59(10): 3928-3942.
  39. Jager, A. and Span, R., *Equation of State for Solid Carbon Dioxide Based on the Gibbs Free Energy. Journal of Chemical and Engineering Data*, 2012. 57: 590-597.
  40. Yokozeki, A., *Solid-Liquid-Vapor Phases of Water and Water-Carbon Dioxide Mixtures Using a Simple Analytical Equation of State. Fluid Phase Equilibria*, 2004. 222-223: 55-66.